Investigation of systematic errors in the Bottom-Up analysis method for laser produced tin plasmas

Utilizing simulated and experimentally obtained retarding field analyzer time-of-flight data

Examinator: Dr. O.O. Versolato

Second examinator: Dr. J. Sheil

Daily supervisors: L. Assink, D.J. Engels, Y. Mostafa

Author: Xyoisan Danser

Student Number UvA/VU: 10764232/2585726

Master Project Physics and Astronomy, size 60 EC
Conducted between 04-09-2023 and 23-07-2024

Universiteit van Amsterdam/Vrije Universiteit
ARCNL
EUV Plasma Processes Group
Amsterdam, The Netherlands

23-07-2024

Contents

Acknowledgments

The thesis that you have in your hands (if you are not reading this from a computer screen) bears a single name in the author section. Although I have written the whole thesis myself, I would not like to give the impression that I could done it without the input of others. I am indebted to many people who helped, inspired and challenged me to deliver this work.

First of all, Oscar I would like to thank you for providing me with the research project. You were always receptive to questions and made me feel included in the team from the very beginning. You challenged me to do the best that I could. You pushed me to improve my forward simulations model, presentations, and of course this thesis. You were always willing to offer input and constructive feedback, which I believe led to new insights. I also greatly appreciated my trip to Trieste which was a fantastic way to get more knowledge about plasma physics. Okay I'll be be honest, it was also just great to go to Italy for a week with someone else paying. You got to see my stubborn side sometimes, when our discussions got a bit heated. Fortunately you appreciated my passion to always feel that I am right. I look back at a very fruitful and educational cooperation.

I would also like thank John for being second examiner. In addition to this role you were able to explain some plasma physics to me as a layman when I had questions about ion emission. You never shy away from giving a short impromptu lecture. I appreciate your (annoyingly) large knowledge of the field and of physics in general. Your dry Irish humor also was a delight, thank you!

Sir Isaac Newton said: "if I have seen further [than others], it is by standing on the shoulders of giants". I would like to give a spin on this: "if I have understood the Bottom-Up [method], it is by standing on the shoulders of a Frenchman". Lucas understanding your Bottom-Up code was the focus of my thesis. To be honest I think it took around three months before I understood what most things were supposed to do. You were kind enough to help even after your time at ARCNL was done, whether it was to explain how to connect the RFAs or to give your opinion about potential errors and improvements. I am grateful that I did not have to start from scratch and that you had to go through years of error messages, so I did not have to.

Special thanks also goes out to Luc. I was fortunate to have you as a daily supervisor. You are someone who not only had thought a lot about the Bottom-Up method, but who also had expansive knowledge about the experimental uncertainties of RFAs. In addition to being a great scientist, you are very hospitable and I had the pleasure of sleeping on your inflatable bed twice. But you gave me something even greater than scientific help, you instilled a love of eierballen in me which I will cherish for the rest of my life.

My other daily supervisor Dion also deserves a great amount of gratitude. You are involved in almost everything that goes on in the team, I am always stunned by the amount of work on your plate. In addition to a very busy schedule you took time to help me, to build a model for the forward simulation, to increase the speed of the code and to do experimental tests. You also helped with feedback to my thesis and presentation, your feedback was always insightful and constructive. I do not appreciate that you call me old though..

Not many people have the good fortune to have three daily supervisors. Yahia was my original daily supervisor. You showed me around when I first arrived, made me feel included and explained a lot (patiently). You were a great help getting me started, when I did not know what to do. We had great discussions about the direction of my project which I am eternally grateful for.

My time at ARCNL was challenging, exciting and rewarding, this was in no small part thanks to the team. I would like to thank everyone who I had the fortune to work with at ARCNL. Whether in Amsterdam or Groningen, everyone was always very friendly and willing to help me, thank you all!

I would be remiss to exclude my family and friends. They were also a great source of inspiration, motivation and help. I would like to thank my father Tu-Fu. Thank you for cultivating my inquisitive mind from a young age and for inspiring me to excel in academics. I am extremely grateful to my mother Wendy for always believing in me, offering a listing ear and motivating me. To my sister Thalia, you seem

to be able to do everything you set your mind to. Your hard work and determination are an inspiration to me.

Thank you all, I could not have done it without you!

Abstract

State of the art integrated circuits are produced employing extreme ultraviolet (EUV) nanolithography. EUV photons are obtained from a plasma produced by high intensity laser illumination of tin microdroplets. Tin ions, which can damage costly optics within the EUV machine, are also emitted in this process. Knowledge about the charge state and energy spectra of ions emitted from laser produced plasma (LPP) is of great importance for industrial, high-volume nanolithography. LPP ion current is measured with retarding field analyzers (RFAs). RFA time-of-flight (ToF) data is analyzed using the so-called 'Bottom-Up method'. Data is divided into energy bins containing known charge states, the use of several retarding voltages allows the calculation of cumulative spectra. Subtracting cumulative spectra yields charge-state-resolved ion energy spectra. Measuring with RFAs and the Bottom-Up method can introduce systematic errors, which influence the spectra and calculated energy. Simulations employing predetermined spectra have been performed to investigate the magnitude of these errors. A ToF resolution of 20 ns leads to an underestimated ion energy in simulations due to numerical instability. The underestimation is most pronounced at high kinetic energy thus and higher charge state. The energy regions with the greatest uncertainty in assigned charge state have been identified. These regions are those at the extrema of energy bins. Subdividing the analyzed energy bins and excluding the regions most impacted by the systematics from analysis leads to an improvement in recovered charge-resolved ion energy, with the deviation between input and output decreasing from 2.5 to 1.5 %. This improved analysis method has subsequently been applied on experimental data. The recovered total kinetic energy and momentum increase roughly 1 % and 0.5 % respectively, when compared to the original analysis method. A single experimental dataset has been analyzed using four ToF resolutions by downsampling. The recovered energy is 2.2 % lower using a ToF resolution of 20 ns when compared to a resolution of 2 ns. This decrease is mainly attributable to the decrease in assigned energy of the higher charge states in line with simulated spectra.

1. Introduction

1.1. Photo-lithography

Photo-lithography is a technique employed to inscribe small features using light. Photo-lithography has played a vital role in the production and improvement of integrated circuits (IC), also known as microchips. Over a time span of roughly seven decades photo-lithography has been improved to yield ever decreasing circuit sizes [1]. This reduction in circuit size can be summarized in *Moore's law*, which predicts that the amount of transistors on an (affordable) IC doubles roughly every two years [2].

The current state of the art of photo-lithography is extreme ultraviolet (EUV) nanolithography. Nanolithography is essential for the mass production of the most advanced integrated circuits [3]. The most advanced nanolithography machines employ EUV radiation, with a wavelength of $13.5\,\mathrm{nm} \pm 1\%$, enabling miniaturization of features to the nanometer scale [4, 5].

There is a drive to use ever smaller wavelengths of light to further miniaturize features. This drive towards smaller features is needed to keep Moore's law on track, as smaller features allow more transistors to be imaged per unit area.

The smallest feature size that can be obtained using photolithography, known as the critical dimension (CD), is proportional to the wavelength of light used

$$CD = k_1 \frac{\lambda}{\mathrm{NA}}, \tag{1.1}$$

where k_1 is a coefficient related to the manufacturing process and NA is the numerical aperture of the optics [6]. From Equation 1.1 it can be deduced that, all else being equal, decreasing the wavelength of the light used in photo-lithography, decreases the CD. Increasing NA can also contribute to a reduction is CD, but increases in NA are limited.

1.1.1. Extreme ultraviolet nanolithography

Hot and dense plasma can serve as an efficient source of short-wavelength radiation, such as EUV radiation. EUV radiation can be obtained from tin laser produced plasmas (LPPs) [7], using for instance a CO_2-gas or Nd-YAG solid-state laser to create the plasma [8]. Using a high power laser, focused on a tin target in a vacuum, a hot and highly ionized plasma is created [9]. Currently, in industry the main drive laser is a pulsed CO_2 gas laser with a wavelength of $10.6\,\mu\mathrm{m}$ [2, 8]. This is done, in part, because this laser wavelength minimizes the amount of debris emanating from the plasma [8]. The repetition rate of the laser in industrial nanolithography is roughly 50 kHz [2], this is done to ensure sufficient power output of EUV radiation of at least 545 W in 2π sr [10].

In industrial nanolithography, the element of choice for EUV production is tin (Sn) [5]. Tin is used because tin LPPs have a high intensity emission peak around 13.5 nm [10]. The choice of this particular wavelength for nanolithography can be mainly attributed to the fact that there are no suitable lenses for EUV light. Therefore, the optics used for nanolithography are molybdenum and silicon (Mo/Si) multilayer mirrors (MLM) [2, 11], which optimally reflect around 70% of in-band radiation [5, 8, 12]. In-band radiation is defined as the 2% bandwidth around 13.5 nm [13].

Microdroplets of tin serve as mass-limited targets for a nanosecond pulse length driving laser [14]. The energy of the laser is converted to in-band radiation; however, the laser energy also contributes to dissipation into different energy channels such as out-of-band light emission [8]. Another dissipation channel is (kinetic) energy of debris that get ejected from the LPP, debris can in turn damage the EUV optics, reducing MLM lifetime [5, 8]. The debris emanating from LPPs includes plasma ions, neutral atoms or clusters, and tin droplet fragments [5, 7, 8]. Ions can be seen to be the main concern to the

MLM optics, as at optimal operation the target is almost completely converted into a plasma. These ions are harmful to the MLMs, reducing overall reflectivity and thus energy efficiency and throughput of nanolithography machines [7]. To minimize the generation of debris, the total mass of the target is limited [5].

Different debris mitigation schemes can be used to prevent damage to optics, including deflection with the use of strong magnetic fields and stopping with the use of a background or buffer gas [5, 7], such as H_2 [5, 15]. The choice of buffer gas and its pressure is governed by its transmissivity of EUV and effectiveness in mitigating debris [7]. Current industrial EUV nanolithography mainly employs H_2 gas for stopping and charge exchange (also known as electron capture) as H_2 is a weak absorber of EUV radiation [2, 5]. The deflection using magnetic fields is not widely utilized, as strong magnetic fields are necessary [2] and H_2 is still needed [5].

Charge exchange between positive tin ions and neutral H_2 molecules lowers the charge of the ions, by capturing one or more electrons from the gas. In this process, electrons can also be ejected into the vacuum. The charge exchange cross-sections depend in general on charge-state, relative velocity and electronic structures of the target and the ion [2]. Stopping is the reduction of kinetic energy of ions due to interaction with the buffer gas, at low gas pressures stopping is negligible [7, 16].

One of the most important figures of merit for nanolithography is the conversion efficiency (CE). CE is defined as the plasma emissivity at $13.5\,\mathrm{nm} \pm 1\%$, into a half-sphere ($2\pi\,\mathrm{sr}$) back towards the laser, divided by laser pulse energy [5, 17]. This is an important figure as this is the direction towards the collector MLM [5], which is the first of the optics that guide the EUV light from the target towards the wafer being exposed. In addition to CE, a requirement for industrial, high-volume nanolithography is long lifetime of the collector mirror [17].

In addition to the useful EUV radiation, tin LPPs emit debris, such as ions which can damage or coat the collector mirror [2, 5, 11, 17, 18]. Such damage can be due to coating, sputtering and ion implantation [5, 11, 15]. Whether an ion impinging on the collector mirror will coat, implant or sputter depends on its kinetic energy and charge state [13, 15]. This indicates the importance of research into the energy and charge states of tin ions that are ejected from tin LPPs [5]. CE and emitted debris are both influenced by multiple system parameters, including target geometry and laser parameters. The wavelength of the laser used has a large influence on both CE and debris [17].

The industry places great importance on throughput, which can be simply summarized as the amount of wafers that can be exposed per unit time, e.g., wafers per hour. Damage to the collector mirror can reduce throughput and therefore understanding debris emission and gaining knowledge into mitigating debris is of great importance for industrial high-volume EUV nanolithography.

1.2. Current work

Gaining knowledge about the energy and charge state distribution of ionic debris emanating from LPPs, can give insights into improvements for industrial nanolithography. This includes for instance knowledge about (more) effective mitigation schemes to increase optics lifetime or to inform the choice of laser wavelength, pulse shape, and/or (tin) target shape for next generation nanolithography. At the EUV Plasma Processes (EUVPP) group at the Advanced Research Center for Nanolithography (ARCNL), fundamental research is performed to develop further knowledge into effective and efficient production of EUV radiation. One of the key research directions is examining the emission of tin ions from LPPs. The emission of ions is recorded employing retarding field analyzers (RFAs). Using the so-called 'Bottom-Up method', charge-state-resolved energy spectra can be obtained. The use of multiple RFAs at different recording angles further allows insight into the angular dependence of emission.

In the past the Bottom-Up method has yielded useful data and further insight into the (strongly anisotropic) ion emission from tin LPPs. However, a comprehensive analysis of uncertainties and potential systematic errors is still lacking. This work aims to quantify the relative contributions of different systematic errors and where possible to recommend improvements. The remainder of this thesis is subdivided into the following chapters.

Chapter 2 explains how RFA time-of-flight measurements are taken and what potential systematic effects measuring with RFAs might introduce.

Chapter 3 introduces the Bottom-Up method, explaining how the transformation from RFA time-of-flight data, to charge-state-resolved energy spectra is performed. It also deals with potential systematic effects this analysis method introduces.

Chapter 4 explains simulating RFA time-of-flight data based on predetermined spectra, so-called 'forward simulations'. These allow insight into the effect of systematic effects of RFA measurements on the Bottom-Up method. Different effects are probed independently using these simulations, allowing the quantification of the relative contributions of each effect.

In **Chapter 5** the results of the forward simulations are presented and discussed. The effect of the individual parameters and a combination of parameters are presented.

Chapter 6 deals with the results of experimentally obtained data. Alternative analysis methods are compared which are based on analysis of the performed forward simulations.

Chapter 7 follows with the conclusions. Recommendations are also done for follow-up research and improvements for the method.

For the interested reader a collection of appendices is also included, giving more context and explanation.

This thesis examines and quantifies the relative magnitude of a collection of systematic effects introduced by measuring ion emission from tin LPPs with retarding field analyzers and by the analysis by the Bottom-Up method.

2. Using a retarding field analyzer in time-of-flight mode to calculate kinetic energy

2.1. Experimental setup

A short description of the experimental setup is included as the focus of this thesis is mainly data analysis. For a more in-depth explanation see earlier work, for instance Poirier et al. [15].

A tin reservoir is kept at a constant temperature of 270 °C, above the melting point of tin. The reservoir is mounted above a vacuum chamber which is kept at 10^{-7} mbar [15]. A pressure is applied on the molten tin using argon gas. The molten tin is extruded through a nozzle, creating a flow of tin. A piezo element in the nozzle is used to break up the tin into a steady stream of tin droplets. The droplet size can be tuned by changing the frequency of the piezo. A helium-neon (HeNe) laser focused to a small sheet is used to detect the incoming droplet. As the droplet traverses the laser sheet it reflects light which is recorded by a photo-multiplier tube. The frequency of the photo-signal is down converted to 10 Hz. A high-intensity *main pulse* ($\lambda = 1\,\mu m$ in the current work) laser is shot at the droplet, creating a laser produced plasma (LPP), which emits radiation (including useful, extreme ultraviolet photons) and debris. This debris includes ions, which are recorded using multiple retarding field analyzers.

2.2. Retarding field analyzer

A retarding field analyzer (RFA) is a Faraday cup (FC) behind a retarding potential, that can be used to (selectively) collect charge [6]. A schematic of an RFA is shown in Figure 2.1.

An RFA functions as a high-pass energy filter for charged particles such as ions, where only particles that have sufficient kinetic energy can pass. The RFAs employed in the current work are all of the type *Kimball Physics FC73-A*. These RFAs have 4 grids in front of the FC.

The first grid as seen from outside, is the ground grid. After the ground grid are two retarding grids, followed by a suppressor grid. These three types of grids have different purposes: the ground grid is connected to the ground and ensures that the field lines corresponding to the retarding voltage do not exit the device, ensuring a more isotropic retarding potential. The suppressor grid ensures that unwanted charged particles do not enter the FC, in the context of the LPP experiments of ARCNL, those charged particles are plasma electrons. The suppressor grid also restrains secondary electrons, produced by impact of the ion current on the cup, from exiting the FC. Restraining secondary electrons ensures that ion current is not overestimated. Finally, the retarding grids create the high-pass filter needed to selectively block certain ions.

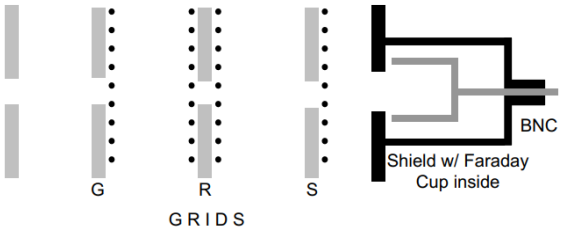

Figure 2.1.: Schematic view of an RFA, from left to right: The ground grid (G), the retarding grids (R) and the suppressor grid (S). Followed by the Faraday cup which connects to a scope using a BNC. Figure reproduced from [19].

As different charge states experience different effective potentials a Sn^{2+} ion will need double the kinetic energy that a Sn^{1+} ion needs to pass. The kinetic energy of a charged particle Sn^{z+} needs to be higher than the effective potential such that

$$E_{\mathrm{kin}} > zeU_{\mathrm{ret}}, \tag{2.1}$$

where z is the charge state of a tin ion (1+, 2+ ...), e is the elementary charge (1.602×10^{-19} C) and U_{ret} is the voltage on the retarding grids.

2.2.1. RFA time-of-flight traces

In the LPP experiments performed at ARCNL, time-of flight (ToF) data is recorded. Time traces of ion current are taken by connecting the RFAs to a transimpedance amplifier. The amplifier is employed to convert from current to a voltage, which can be recorded using an oscilloscope. Traces are recorded at different values of retarding potential ranging from 0 V until the potential at which ion current is no longer visible on the oscilloscope. Typically a maximum of 1000 V is sufficient to block all ion current. An example of ion current for different retarding voltages is shown in Figure 2.2a.

As the retarding voltage is increased, the effective potential for each ion goes up. This causes certain ions to be repelled, decreasing overall ion current. Step-like features appear, which correspond to the minimum energy required for a certain charge state to be passed and thus measured (see Equation 2.1). Figure 2.2a shows that the ion current decreases and that the steps move to shorter times as the retarding voltage is increased. This shift towards shorter times indicates that a higher minimum energy is needed at higher retarding voltage.

Taking a single retarding voltage, we can calculate the effective potential for each charge-state. This allows the assignment of 'exclusive' zones, where only certain charge states can pass. The lowest energy zone can contain only Sn^{1+}, the second energy zone can contain Sn^{1+} and Sn^{2+}, the third can contain Sn^{1+}, Sn^{2+} and Sn^{3+} etc.

As an example, if we apply a retarding voltage of 100 V, no ions below 100 eV pass, as the minimal kinetic energy for a Sn^{1+} needed to pass is 100 eV. In this case the effective potential for an ion is 100 eV multiplied by the charge state (thus for a Sn^{2+} the potential barrier is 200 eV, for a Sn^{5+} it is 500 eV). For energies between 100 and 200 eV therefore, only Sn^{1+} ions can pass. Calculating the time-of-flight that corresponds to 100 and 200 eV allows the assignment of the exclusive time zone of Sn^{1+} ions. The same can be done for 200 to 300 eV, where only Sn^{1+} and Sn^{2+} can pass. This useful fact is later used to calculate cumulative ion spectra, which play a pivotal role in the Bottom-Up method, which is further discussed in Chapter 3.

2.3. Transmission of an RFA

In general the transmission of a gridded RFA is unknown, as it has been found that the relative orientation of the grids is not the same between devices. Work has been done in the past to simulate the transmission using *SIMION* [20]. Simulations were performed with a mono-energetic, single isotope beam.

2.3.1. Geometric transmission

First of all, we can consider the geometric transmission. The transmission of an RFA is equal to the geometric transmission, when no potentials are applied on the grids. The geometric transmission depends heavily on the relative position of the grids, which can lead to a transmission ranging from roughly 40 to 80% for minimal and maximal grid overlap respectively [20]. The geometric transmission of a single grid of the Kimball FC73-A, T_0, is around 82% or 0.82, if we have 4 randomly placed grids the expected geometric transmission is $T_4 = T_0^4 \approx 0.45$ while the transmission of two grids, i.e. when all ions pass the two retarding grids is: $T_2 = T_0^2 \approx 0.67$.

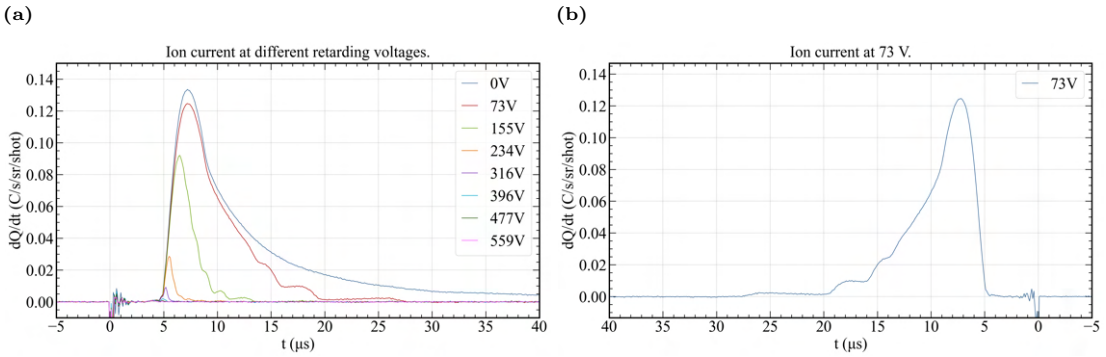

Figure 2.2.: Examples of experimentally recorded ion currents, at t = 0 a photo-electron peak is observed. Step-like additions in current are visible as we move towards shorter time-of-flight (ToF), corresponding to additional charge state being able to pass the potential barrier. Eight time-of-flight traces are shown in (a), as the retarding voltage is increased the cut-off for all charge states moves to shorter times and the total current decreases. (b) shows a single trace at a retarding voltage of 73 V. The time-of-flight axis is inverted to represent the increase in kinetic energy corresponding to decreasing ToFs. Due to the effective potential experienced by each charge-state, exclusive zones are present, where only Sn^{1+} ions can pass (27 to 18 µs), followed by a zone where Sn^{1+} and Sn^{2+} can pass (18 to 15 µs), then Sn^{1+}, Sn^{2+} and Sn^{3+} (15 to 13 µs) etc.

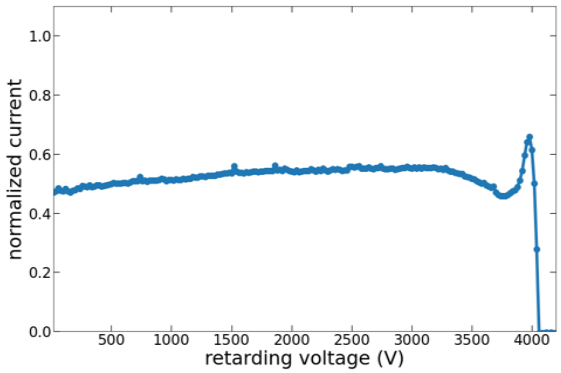

Figure 2.3.: Ion transmission as a function of retarding voltage for a mono energetic beam with a kinetic energy of of 4 keV. An increase in transmission can be observed when the effective retarding potential and kinetic energy become similar, which is caused by strong ion lensing. Figure courtesy of Luc Assink, reproduced from experiments performed at the *Rijkuniversiteit Groningen*.

2.3.2. Potential dependent transmission function

The *SIMION* simulations reveal that in addition to the geometric considerations, that the transmission function depends on the charge state, initial kinetic energy, and the potentials that are applied on the grids. This is due to 'lensing', where the trajectory of charged particles is changed when passing the grids. A representative example of a (experimentally obtained) transmission function can be seen in Figure 2.3.

As discussed above, the transmission function for different RFAs and different charge states can vary substantially. One persistent feature however is an increased transmission for ions that barely pass the potential barrier, which can be seen in Figure 2.3 around 4 keV. This is caused by the fact that ions, with

energies close to the effective potential, experience strong lensing. These ions are just able to overcome the retarding potential and are repelled from the retarding grids towards the middle of the grids. This causes almost all ions of these energies to pass the retarding grids, such that the effective transmission resembles the geometric transmission of two instead of four randomly placed grids [20].

A correction is performed for transmission, assuming the geometric transmission of four grids T_4. However, this correction factor underestimates the transmission for the ions with kinetic energies close to the effective potential. Applying the correction factor for the transmission of four grids

$$\hat{T_2} = \frac{T_2}{T_4} = \frac{0.67}{0.45} \approx 1.48. \tag{2.2}$$

It is thus likely that ion current in the region where ions barely pass the potential barrier is overestimated by roughly 50%, if T_4 is used as a correction factor.

2.4. RFA time-of-flight resolution due to isotopes

In the LPP experiments performed by the EUVPP group at ARCNL, the kinetic energy of tin ions is not directly measured. Rather, kinetic energies are inferred from the time-of-flight (t), abundance weighted average mass ($\bar{m}$) and length of flight of the ions (L), see Equation 2.3.

$$E_{\text{kin}} = \frac{1}{2}\bar{m}v^2 = \frac{\bar{m}L^2}{2t^2}. \tag{2.3}$$

As tin has ten naturally occurring isotopes [15], even a mono-energetic beam, e.g. where all ions have a kinetic energy of 100 eV, will lead to a spread in ToF due to mass differences between isotopes. As we use the time-of-flight to infer the kinetic energy, this can have an effect on which energy we assign to an ion. For instance, the inferred energy for an ion of 100 eV is 95.8 eV and 106.1 eV for the most and least massive isotope of tin respectively.

The Bottom-Up method uses cutoff times based on the abundance weighted mean mass. However, at increasing charge state this does not allow us to distinguish charge states. The cutoff time for the heaviest Sn^{10+} is later than the lightest Sn^{11+}. Time of flight can not be used to distinguish charge states of tin of ten and higher. A further discussion of the limit in distinguishable charge state is further discussed in Appendix A.1.

2.5. Energy resolution of an RFA

An implicit assumption using an RFA is that a perfect isotropic potential barrier is present when applying a retarding potential on the grids. This barrier blocks all ions that have an energy lower than the applied (effective) retarding potential and passes all those whose energy is higher than that potential. However, simulations using *SIMION* have shown that this assumption is not completely valid.

In Figure 2.4b it can be observed that some Sn^{1+} ions with an initial energy slightly lower than 100 eV, pass the retarding voltage of 100 V. This is due to the potential 'sagging' between the grids, resulting in a potential slightly lower than on the grids themselves. This means that an ion with 95 eV incident on the centre of a grid square can pass. Potential sag is schematically shown for a single retarding grid in Figure 2.4a. Using two retarding grids ensures a more isotropic potential and thus a less sag, but the effect can not be entirely remedied [20].

The energy resolution fit used in Figure 2.4b is a Gaussian cumulative distribution function (GCDF). One of the variables of a GCDF is the FWHM (Full Width at Half Maximum). A small FWHM means that little potential sag occurs, while a large value corresponds to more sag. A large value of FWHM is undesirable.

The value of the FWHM in general depends on the specifics of the RFA, such as pitch and the width of the grids. In the simulation the specifics of the Kimball FC73-A have been used. The value of the FWHM in Figure 2.4b: 0.011 corresponds to 1.1 % of the effective retarding voltage multiplied by the elementary charge e, in the current case that is 1.1 eV ($= 100\,\text{V} \cdot 1.1\,\% \cdot e$).

(a) **(b)**

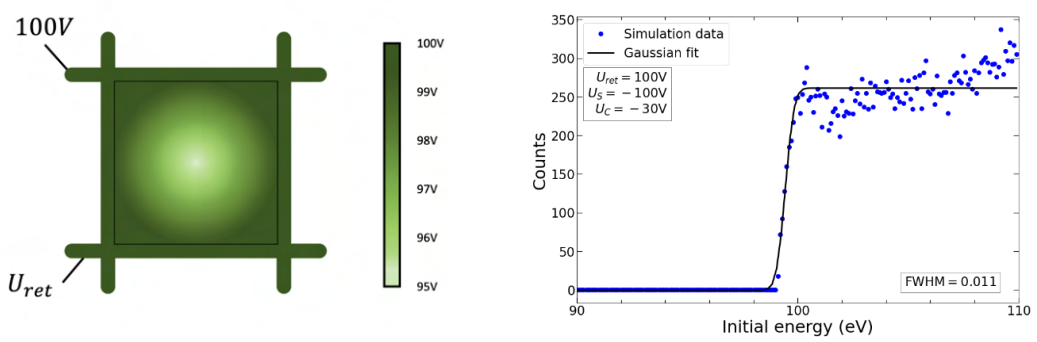

Figure 2.4.: (a) shows a schematic of a spatial potential profile using a single retarding grid. A retarding potential of 100 V is applied on the retarding grid, however between the grids the potential is lower, it 'sags'. This allows some ions of energy lower than the applied potential to pass. (b) shows the simulated energy resolution of an RFA using *SIMION*. The non step-like energy resolution is due to the potential sag shown in (a). Both figures reproduced from Assink [20] with permission.

2.6. Drift and acceleration

In an RFA, electrostatic fields are present between the different grids. Due to the finite distance between grids these fields can decelerate or accelerate charged particles such as ions. This can lead to a time-of-flight that is larger or smaller than the potential free time-of-flight. The former is known as drift, while the latter can be called acceleration. The ToF is used in to calculate/infer (initial) kinetic energy. Thus drift and acceleration can lead to an over- or underestimation of initial ion kinetic energy. The magnitude of this effect is based on the specific RFA design, ion charge-state, initial kinetic energy and exact potentials applied on all grids and on the FC. For most ions the percentage change in ToF is less than 5 %, however for a small fraction of ions the change will be substantially higher. Drift is dominant for ions with a kinetic energy that is very similar to the effective potential. Appendix A.2 provides a more in-depth explanation of drift and acceleration.

3. Bottom-Up method

3.1. Bottom-Up explained

Analysis of the tin ion current is performed using the so-called Bottom-Up method. This is an analysis method that was developed and employed at ASML and ARCNL [21] to obtain the energy spectra of different charge states of (tin) ions.

An RFA is used to record ToF traces of ion current at different retarding voltages. The ToF of ions is transformed the corresponding kinetic energy to obtain ion energy spectra. By using multiple RFAs aligned at different angles with respect to the incoming laser pulse, it is possible to obtain angularly resolved ion energy spectra.

Ion current is recorded by multiple RFAs via a voltage that is read out from an oscilloscope. This voltage is transformed to a current by dividing by the amplifier gain. The current is corrected for solid angle covered by the RFA aperture and transmission. In practice we obtain: $\frac{d^2Q}{dtd\Omega}$, where $d\Omega$ is the solid angle covered by the RFA aperture. Strictly speaking, all (ion) current terms: ($\frac{\mathrm{d}Q}{\mathrm{d}t}$, $\frac{\mathrm{d}Q}{\mathrm{d}E}$, $\frac{\mathrm{d}N}{\mathrm{d}E}$ etc) are thus per steradian. By interpolating between the measured angles an approximation of the complete 4π sr ion emission can be made. This is used to approximate the total ion number, energy and momentum. This solid angle dependence will be omitted in this work for brevity, for more information see Poirier et al. [18].

The time domain ion current $\frac{\mathrm{d}Q}{\mathrm{d}t}$ can be expressed in the energy domain by the identity [15]

$$\frac{\mathrm{d}Q}{\mathrm{d}E} = \frac{\mathrm{d}Q}{\mathrm{d}t}\frac{\mathrm{d}t}{\mathrm{d}E} \tag{3.1}$$

where we assume constant velocity over the whole ToF [20].

The distance that an ion has to cover to reach the RFA from the plasma, L, is known, thus (to first approximation, for more information see Appendix A.2) we can directly relate the time-of-flight, t, to the velocity of the ions

$$v = \frac{L}{t}. \tag{3.2}$$

Clearly knowing the velocity also allows us to calculate the kinetic energy of the ions

$$E_{\mathrm{kin}} = \frac{1}{2}mv^2 = \frac{mL^2}{2}\frac{1}{t^2}, \tag{3.3}$$

where m is the isotope abundance weighted average mass of tin [15]. Rewriting Equation 3.3 to obtain an expression for time-of-flight

$$t^2 = \frac{mL^2}{2E}, \tag{3.4}$$

$$t = L\sqrt{\frac{m}{2E}}. \tag{3.5}$$

Taking the (absolute value of the) derivative with respect to energy

$$|\frac{\mathrm{d}t}{\mathrm{d}E}| = L\frac{\sqrt{m}}{2\sqrt{2}}\frac{1}{E^{\frac{3}{2}}} \propto E^{-\frac{3}{2}}, \tag{3.6}$$

which is the conversion factor needed to obtain the energy domain current.

Using different values of retarding voltage, U_{ret}, it is possible to reject certain ions. Ions are rejected if their kinetic energy E_{kin} is smaller than the effective potential experienced by the ion. The effective potential for an ion with charge state z, Sn^{z+}, is

$$U_{\mathrm{eff}} = zeU_{\mathrm{ret}}. \tag{3.7}$$

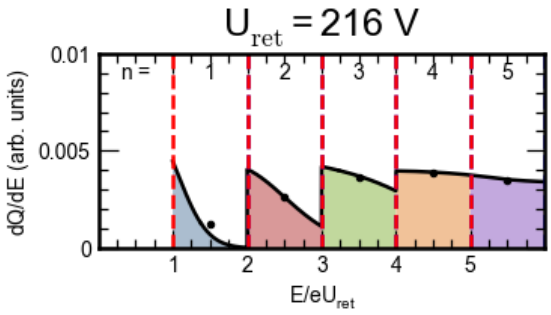

Figure 3.1.: Schematic example of binning, the red dashed lines are located at multiples of eU_{ret}. These correspond to the minimum energies needed for the charge state $z = n$ to pass the potential barrier. The n^{th} bin can contain charge states equal or lower than n. As an example, the $n = 3$ bin can contain all charge states up to and including 3. The black markers correspond to the mean current contained within a bin.

Thus, ions with

$$E_{\text{kin}} \leq zeU_{\text{ret}} \tag{3.8}$$

are repelled. We can use this fact to obtain an energy spectrum of all relevant charge states. For each retarding voltage, the total energy domain is split into bins of width eU_{ret}, which correspond to the 'exclusive' zones discussed in Section 2.2. The bins are numbered by an index n ($\in \mathbb{N}^+$), which corresponds to the highest charge state that can be present in that bin. The n^{th} energy bin is centered on

$$E_n = (n + \frac{1}{2})eU_{\text{ret}} \tag{3.9}$$

with the bin spanning from neU_{ret} to $(n + 1)eU_{\text{ret}}$. A schematic example of binning is shown in Figure 3.1.

To see why n is the highest possible charge state in a bin, we use the fact that only ions with energy above the effective potential are passed,

$$E > zeU_{\text{ret}}, \tag{3.10}$$

and the fact that to be contained in the n^{th} bin the energy must be

$$neU_{\text{ret}} \leq E < (n + 1)eU_{\text{ret}}. \tag{3.11}$$

It follows that only ions with $z \leq n$ can end up in the n^{th} bin. This useful fact can be used to construct cumulative spectra that contain certain charge states. This is done by taking the mean value of ion current in a bin and assigning it to the energy at the midpoint of the bin, E_n. The mean current is obtained by taking a numerical (trapezoidal) integral of current and dividing by the width of a bin. In Figure 3.1 the mean values of current are shown by the black markers.

Taking measurements at M unique retarding voltages, we assign M values of average current to M values of E_n, yielding cumulative spectra, which are numbered with an index n. The nth cumulative spectrum can contain Sn^{1+}, ..., Sn^{n+}. The $z = 1$ spectrum is immediately recovered from the spectrum of the $n = 1$ bins, as this bin can only contain $z = 1$ ions. Having obtained the $z = 1$ spectrum we can subtract cumulative spectra, subtracting the $(n - 1)^{\text{th}}$ spectrum from the n^{th} spectrum to obtain the spectrum of $z = n$.

To be more concise, we can use the obtained spectrum of $n = 1$ (which is the same as that of $z = 1$) to find the spectrum of $z = 2$. This is done by subtracting the $n = 1$ spectrum from the $n = 2$ spectrum (which contains the cumulative spectrum of $z = 1, 2$) to obtain the $z = 2$ spectrum. Subsequently, the cumulative spectrum of $z = 1, 2$ ($n = 2$) is subtracted from the cumulative spectrum of $z = 1$, 2, 3 ($n = 3$) spectrum to obtain the $z = 3$ spectrum. This is done until all relevant charge states have been included.

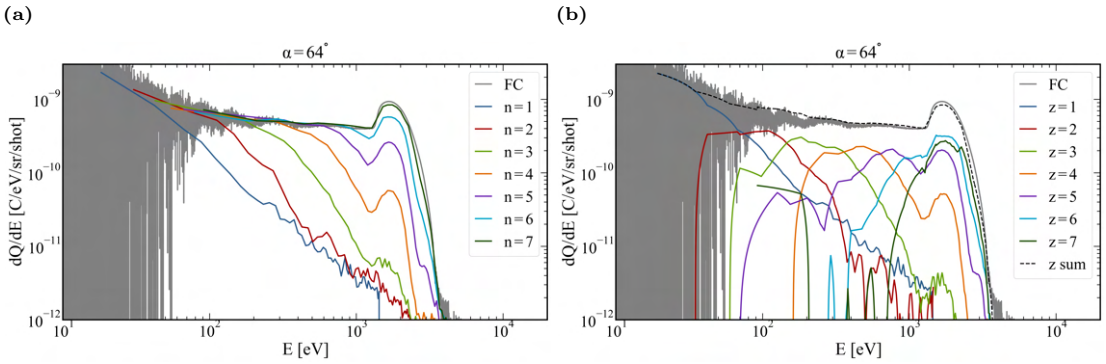

Figure 3.2.: Example of cumulative (a) and charge-state-resolved (b) $\frac{\mathrm{d}Q}{\mathrm{d}E}$ spectra, obtained using the Bottom-Up method. Measurement is taken at an angle of 64° w.r.t. the laser. In (b) the sum of the individual charge states is shown as 'z sum'. The charge state sum closely resembles the Faraday Cup (FC) like measurement. The FC is a measurement taken without retarding potential.

In general

$$\frac{\mathrm{d}Q_z}{\mathrm{d}E} = \frac{\mathrm{d}Q_{n=z}}{\mathrm{d}E} - \frac{\mathrm{d}Q_{n=z-1}}{\mathrm{d}E} \tag{3.12}$$

where $\frac{\mathrm{d}Q_z}{\mathrm{d}E}$ is the charge-state-resolved energy spectrum containing only Sn^{z+} and $\frac{\mathrm{d}Q_{n=z}}{\mathrm{d}E}$ is the cumulative spectrum, containing Sn^{1+}, ..., Sn^{z+}.

An example of experimentally obtained cumulative spectra is shown in Figure 3.2a, where the cumulative spectrum $\frac{\mathrm{d}Q_{n=7}}{\mathrm{d}E}$ closely resembles the FC measurement. The corresponding charge-state-resolved spectra obtained by the Bottom-Up method are shown in Figure 3.2b. Summing the individual charge-state-resolved spectra yields the charge state sum spectrum ('z sum'), this should match the total ion current with no retarding voltage, this is shown in Figure 3.2b as the 'FC measurement'. A good agreement is found, indicating that total ion current can be reconstructed employing the charge-state-resolved spectra obtained by the Bottom-Up method.

3.1.1. Ion number energy distributions

Having obtained charge-state-resolved spectra, we can divide each spectrum by the charge of a single ion to obtain charge-state-resolved ion number energy distributions

$$\frac{\mathrm{d}N_z}{\mathrm{d}E} = \frac{1}{ze}\frac{\mathrm{d}Q_z}{\mathrm{d}E}, \tag{3.13}$$

where e is the elementary charge. These distributions further allow us to obtain the total ion number energy distribution,

$$\frac{\mathrm{d}N}{\mathrm{d}E} = \sum_{z=1}^{z_{\max}} \frac{\mathrm{d}N_z}{\mathrm{d}E}, \tag{3.14}$$

which in turn can be used to calculate many figures of interest such as total ion number

$$N_{tot} = \int \frac{\mathrm{d}N}{\mathrm{d}E} dE', \tag{3.15}$$

total ion kinetic energy

$$E_{\mathrm{tot}} = \int E' \frac{\mathrm{d}N}{\mathrm{d}E} dE', \tag{3.16}$$

and total (radial) ion momentum

$$p_{tot,r} = \int p_r(E') \frac{\mathrm{d}N}{\mathrm{d}E} dE'. \tag{3.17}$$

where the radial ion momentum is given by $p_r(E) = \sqrt{2mE}$ [18]. The charge-state-resolved ion number energy distributions can be used to calculate the corresponding charge-state-resolved figures.

3.2. Potential errors

The rest of this chapter will deal with potential systematic effects and errors that might be included by using the Bottom-Up method. Where applicable, suggestions will also be done to decrease/mitigate these effects.

3.2.1. Misplaced ions due to isotope mass

For a given kinetic energy a spread in ToF is present due to isotope masses. When binning, ion less massive than the mean arrive 'early', while ions that are more massive arrive 'late'. This can lead to the most massive isotopes being placed in a bin that is lower than what they correspond to, this can lead to 'isotope contamination'.

As an example, if we have a retarding voltage of 100 V, and a Sn^{2+} ion that weighs 123.9 u (most massive tin isotope), with a kinetic energy of 205 eV, and a length of flight of 1 m, then its time-of-flight is given by:

$$t = 1\,\mathrm{m} * \sqrt{\frac{123.9\,\mathrm{u}}{2 * 205\,\mathrm{eV}}} = 55.9\,\mu\mathrm{s}. \tag{3.18}$$

However the maximum time for the second bin is given by the mean weight of 118.71 u which corresponds to a time-of-flight of

$$t_{\max}(z=2) = 1\,\mathrm{m} * \sqrt{\frac{118.71\,\mathrm{u}}{2 * 200\,\mathrm{eV}}} = 55.5\,\mu\mathrm{s}. \tag{3.19}$$

Thus the Sn^{2+} with an energy of 205 eV will be assigned at an inferred energy lower than its actual energy. The assigned energy is calculated with the mean mass

$$E_{\mathrm{assign}} = \frac{1}{2}\bar{m}(\frac{1\,\mathrm{m}}{55.9\,\mu\mathrm{s}})^2 = 196.9\,\mathrm{eV}. \tag{3.20}$$

By assumption, only Sn^{1+} should be able to be detected with this assigned energy. Our Sn^{2+} ion will therefore assigned to the spectrum of Sn^{1+}, while it should contribute to the cumulative spectrum containing Sn^{2+} as its kinetic energy is contained in the second bin which contains kinetic energies of 200 to 300 eV. In this way 'slow' massive ions can contaminate spectra of lower charge states, leading to an overestimation in the lower charge state and by subtraction of cumulative spectra to an underestimation in the higher charge-state.

3.2.2. Broadening of spectra and reduction of peak height

A potential error introduced by the use of energy bins is that the average of ion current is taken over the whole energy range of a bin. This current is assigned to the middle of the bin, as an example: using a retarding voltage of 1 kV, the $n = 1$ bin will span from 1 to 2 keV. The average current in this bin will be assigned to 1.5 keV. However, if the maximum energy that ions have is 1.001 keV, current still gets assigned to an energy of 1.5 keV. Thus, the energy of fast ions can be overestimated by at most 50 % in the $n = 1$ bin. A schematic example of energy overestimation is shown in Figure 3.3a.

Conversely, consider the situation where the lowest energy that an ion has is 9.99 eV. Using a retarding voltage of 5 V, the $n = 1$ bin will span from 5 to 10 V. The ion current at 9.99 eV will be included and current will be assigned to 7.5 eV, where no actual current is present. Thus, the Bottom-Up method underestimates the energy of the slowest ions in the $n = 1$ bin by at most 25 %. A schematic example of lowest energy underestimation is shown in Figure 3.3b. Overestimation of highest energy and underestimation of lowest energies lead to an artificial broadening of spectra.

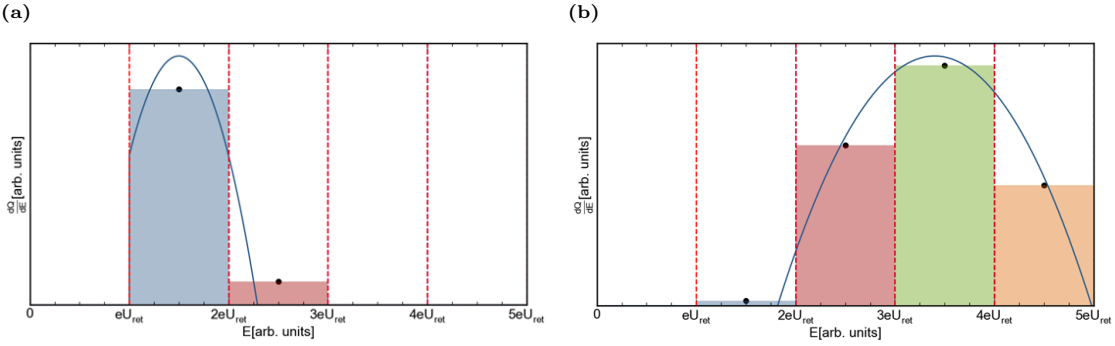

Figure 3.3.: Schematic illustrations of binning ion current, the ion currents are shown as blue curves. The Bottom-Up method assigns the average current (coloured shading) contained within a bin to the midpoint (black dots). This can lead to an overestimation of the highest energy of a given charge state, which can be seen in (a). In (b) it can be observed that the lowest energy of a given charge state can also be underestimated.

In addition to broadening, binning can also lead to an underestimation in peak height, due to the fact that the mean value of current is assigned, see Figure 3.4a. The mean value can only be lower, or equal to the peak value. As cumulative spectra are subtracted to obtain charge-state-resolved spectra, this can lead to incorrectly assigning current to Sn^{2+} which in reality was due to Sn^{1+} for instance.

The goal of the Bottom-Up method is to construct charge-state-resolved spectra, as accurately as possible. We immediately obtain the $\frac{\mathrm{d}Q_{z=1}}{\mathrm{d}E}$ spectrum from the $\frac{\mathrm{d}Q_{n=1}}{\mathrm{d}E}$ as the latter spectrum can only contain Sn^{1+} ions. We subtract the $\frac{\mathrm{d}Q_{n=1}}{\mathrm{d}E}$ from the $\frac{\mathrm{d}Q_{n=2}}{\mathrm{d}E}$ to obtain the $\frac{\mathrm{d}Q_{z=2}}{\mathrm{d}E}$ spectrum. However, we can see that we run in to trouble if our cumulative spectra are artificially widened due to binning, as then the subtraction will lead to incorrectly assigning current. The $\frac{\mathrm{d}Q_{n=1}}{\mathrm{d}E}$ spectrum is the most affected by this broadening, in the worst case the overestimation in highest energy and underestimation in lowest energy can be 50 % and 25 % respectively. Similarly, the reduction of peak height can also lead to incorrectly assigning current to higher charge states, as we subtract a reduced peak from subsequent cumulative spectra.

Sub-binning

A novel solution to broadening of spectra an reduction of peak height is presented here, this solution was co-developed with Luc Assink. Broadening of spectra and reduction of peak height can be mitigated by subdividing the bins into K smaller 'sub-bins' of width $\frac{eU_{\mathrm{ret}}}{K}$, this has the benefit that the average value of current is assigned to energies that are closer to their actual energy. An example of this is shown in Figure 3.4. We can see that the underestimation/overestimation goes down, in general the maximum over- and underestimation in energy are given by:

$$\Delta E_{\mathrm{max}} = \frac{1}{2K} eU_{\mathrm{ret}}. \tag{3.21}$$

Furthermore, the maximum error in assigned energy can also be expressed as a fraction of the actual energy. As bin n spans from neU_{ret} to $(n+1)eU_{\mathrm{ret}}$ the overestimation of the lowest energy contained in the bin, neU_{ret}, is given by:

$$\frac{\Delta E}{E_{\mathrm{min}}} = \frac{eU_{\mathrm{ret}}}{2KneU_{\mathrm{ret}}} = \frac{1}{2Kn} \tag{3.22}$$

analogously the underestimation of the highest energy contained in the bin, $(n+1)eU_{\mathrm{ret}}$ can be expressed as:

$$\frac{\Delta E}{E_{\mathrm{max}}} = \frac{eU_{\mathrm{ret}}}{2K(n+1)eU_{\mathrm{ret}}} = \frac{1}{2Kn+2K} \tag{3.23}$$

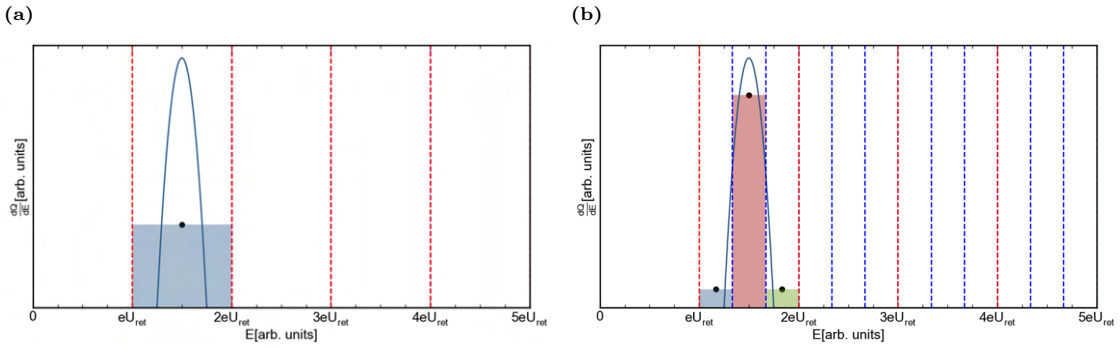

Figure 3.4.: Schematic examples of original binning (a) and sub-binning (b). Using sub-bins ensures that charge/ion current is assigned closer to the actual energy and that the assigned current at that energy more closely represents the actual current.

From Equation 3.22 and 3.23 it can be deduced that higher bins benefit less from sub-binning as the percentage of maximum over- and underestimation is inversely proportional to bin number n. Using these equations, the maximum overestimation with no sub-binning (K = 1) is 50 % and the maximum underestimation is 25 %, these values match the ones found earlier. Note that these percentages represent the worst case, which is all ion current at only exactly the highest or lowest energy contained in a bin, in practice this theoretical upper limit will not be reached.

To increase the resolution in energy and current, sub-binning can be applied, this is schematically shown in 3.4. It can be observed that the individual assigned current (black dots) more closely resemble the input which corresponds to a higher fidelity in output spectra. The total number of sub-bins is limited by the time resolution of the measurement, as numerical integration is employed to calculate average current. If too few points are include in a (sub-)bin this can lead to numerical instability, underestimating current.

4. Forward simulations

Experimentally it is difficult to probe the validity of the recovered charge-state-resolved spectra, which are obtained from the Bottom-Up method. Earlier work cross calibrated the Bottom-Up obtained spectra, with spectra obtained from electrostatic analyzers, yielding a good agreement [15]. However, we do not know in general what the spectra (should) look like. To investigate the validity of the outputs of the Bottom-Up method, so-called 'forward simulations' are performed.

In the forward simulations predetermined energy spectra are defined, and subsequently the retarding effect of an RFA is simulated. From these retarded spectra, simulated time-of-flight data is obtained, which serves as the input for the Bottom-Up method. This allows us to compare our known input spectra to the recovered spectra from the Bottom-Up method. As a first test, an ideal measurement is simulated, with perfect energy resolution, no noise, a single isotope and a flat transmission. As the input spectra are known, from this we can get an order of magnitude of the error introduced by the Bottom-Up method. Subsequently, different systematic effects are included, allowing examination of each effect in isolation, thereby gaining knowledge about the relative contributions of these effects on our experimental measurements.

4.1. Simulated spectra

To simulate spectra displaced Maxwellian functions are employed. Tallents [9] discusses fitting displaced Maxwellian distributions to LPP ion velocity spectra although the spectra are not perfectly Maxwellian, a velocity spectrum similar to a displaced Maxwell distribution is obtained. Burdt [22] uses a Maxwellian fitting function on experimental data to obtain the position of the peaks in $\frac{\mathrm{d}N_z}{\mathrm{d}E}$ of the charge-state-resolved energy spectra, yielding a close fit. The simulated spectra are therefore modelled as displaced Maxwell distributions.

From previous experimental work and simulations [11, 15, 18, 21] as well as from Figure 4.1a it can be observed that a singularly peaked, ion number energy distribution ($\frac{\mathrm{d}N_z}{\mathrm{d}E}$), cannot always accurately describe the physical reality, as secondary peaks are present for higher charge states. The similar position of the secondary peaks for different charge states is explained by the ion bunching concept introduced by Hemminga et al. [11]. Therefore, to simulate the input spectra for our forwards simulations, a secondary Maxwell distribution is included for charge states above Sn^{2+}, with the peak located around 3.5 keV. Figure 4.2a shows the input spectra for our simulation. For example, charge state $z = 4$ has a primary peak at approximately 1.1 keV, while its secondary peak can be seen to be around 3.5 keV.

The predetermined spectra are shown in Figure 4.2a on a log/lin scale. The highest included charge state is $z = 7$ in line with experimentally observed spectra using a 1 um main pulse laser on a droplet target. Figure 4.2b shows the simulated effect of applying a retarding potential on the predetermined spectra. The effective potential (see Equation 3.7) is applied for each charge state. Only the ion current that corresponds to kinetic energies higher than the effective potential (see Equation 3.8) contribute to the measured ion current. From simulated retarded spectra a charge state sum (black dashed line in Figure 4.2b) is calculated and from this time-of-flight data is simulated, an example of which is shown in Figure 4.3. At this point all explicit information about charge states is lost, the information is only implicitly encoded in the step-like charge state additions in current. This ToF data is fed into the Bottom-Up code, with the goal to recover the input spectra. The results of the performed simulations are shown and discussed in Chapter 5.

4.2. Oscilloscope resolution

To model measurement with an oscilloscope, initially all simulated ToF traces are limited to the (originally) used scope resolution. Experimentally, ToF traces are taken for 200 µs, with 10.000 points, yielding a time

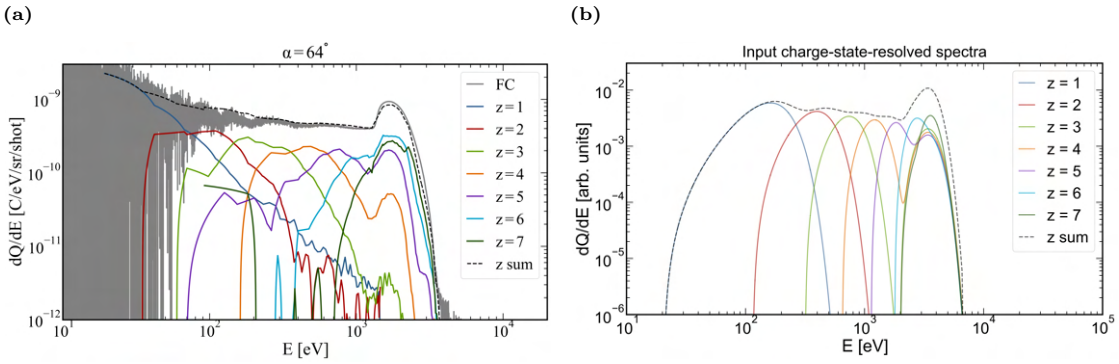

Figure 4.1.: An example of an experimentally obtained spectrum (a) and the input spectra for forward simulations (b). Note the logarithmic/logarithmic scale.

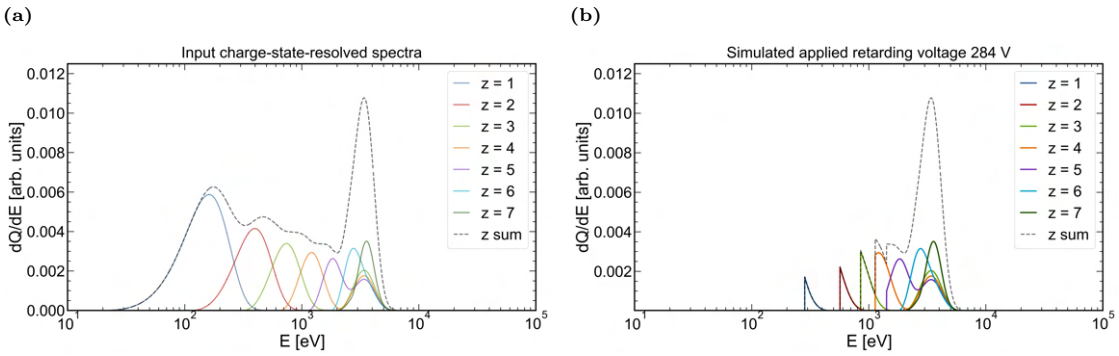

Figure 4.2.: Input spectra for forward simulations (a) and an example of retarded spectra with retarding voltage 284 V (b). Ions with kinetic energies below the effective potential $U_{\text{eff}} = zeU_{\text{ret}}$ do not contribute, thus for Sn^{1+}, ion current below 284 eV (1 * e * 284 V = 284 eV) is zero. For Sn^{2+}, no ions below 568 eV contribute etc. Note the linear/logarithmic scale.

resolution of 20 ns. This can ultimately influence the amount of measurement points that are assigned to an energy (sub-)bin. The analysis method assigns the beginning and end of each (sub-)bin to the ToF within the bin which is closest to the cut-off time, which can lead to numerical instabilities when using an increasing amount of sub-bins, and/or at high energies.

4.3. Energy resolution function

4.3.1. Step function

For the idealized simulated measurement, the implicit assumptions about RFAs are followed, namely that the RFA is a (perfect) high-pass energy filter. In which case only ions with a kinetic energy higher than the effective potential pass (see Equation 3.8). The energy resolution is perfect, and the energy resolution can be modeled as a step function

$$T(E) = \begin{cases} c & \text{E} > U_{\text{eff}} \\ 0 & \text{E} \leq U_{\text{eff}}, \end{cases}$$

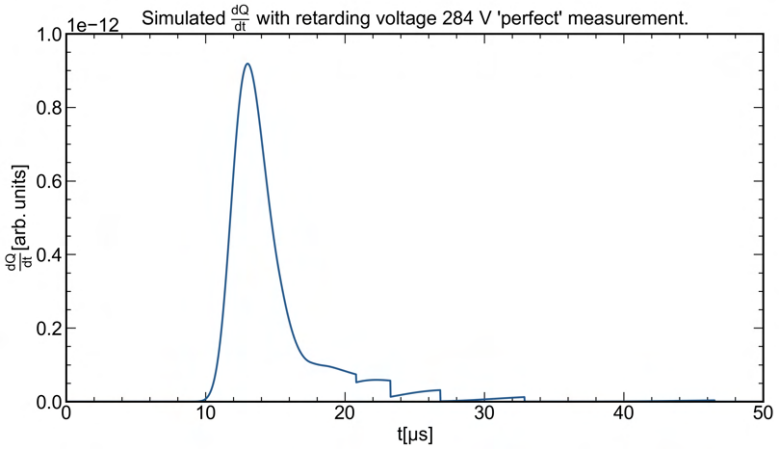

Figure 4.3.: Simulated $\frac{\mathrm{d}Q}{\mathrm{d}t}$ at 284 V, the steps correspond to additional charge states passing the potential barrier. Obtained by transforming the charge state sum in Figure 4.2b into time-of-flight. Note that low values of time correspond to high energy and vice versa.

with $0 \leq c \leq 1$. These restraints are simply due to physical considerations, as at most 100% of ions can pass. Figure 4.3 shows an example of a step function energy resolution.

4.3.2. Gaussian cumulative distribution function

In reality the energy resolution function is more complicated than a simple step function. As discussed earlier, simulations show that the retarding potential between the grid lines 'sags'. Due to this spatial dependence ions with slightly lower energy, than expected from the applied potential, can pass if they are incident on the middle of the grid square. The energy resolution function of a RFA with grids can be approximated by a Gaussian cumulative distribution function (GCDF) [20]. This leads to the motivation to use a GCDF as a energy resolution function in the forward simulations. Assink [20] found that for a Kimball FC73-A with 4 grids (1 ground, 2 retarding and 1 suppressor), the FWHM of the Gaussian function is given by 1.1% of the effective potential. A second value of FWHM is investigated in the forward simulations, namely 2%, corresponding to the theoretical value of an RFA with a single retarding grid. The use of a single retarding grid is being considered as drift (see Appendix A.2) is greatly reduced using a single retarding grid. This reduction in drift however this is at the cost of energy resolution.

4.4. Isotopes

To investigate the effect of the difference in mass between isotopes, the forward simulations allow for the inclusion of a single or all isotopes. If a single isotope is chosen, the simulated $\frac{\mathrm{d}Q}{\mathrm{d}t}$ traces are based on a single mass, which is the abundance weighted mass of tin, 118.71 u. If isotopes are included, ToF data is calculated for each individual isotope mass. These time-of-flight traces are summed, weighted by their relative natural abundance. The result is shown in Figure 4.4, note the slight difference in ToF cutoff due to difference in mass. The sum of $\frac{\mathrm{d}Q}{\mathrm{d}t}$ traces is taken as the input for the Bottom-Up.

4.5. Transmission function

To model the observed increase in transmission for ions that barely pass the potential barrier due to lensing (see Figure 2.3), an energy region of increased transmission is simulated. The width of this region is a fraction of the retarding potential, in the forward simulations two values of increased transmission width are investigated, namely 5 % and 10 %. The former is similar to the experimentally observed value. For these simulations ions with an energy of 100 to 105 % or 100 to 110 % of the effective retarding potential experience increased transmission.

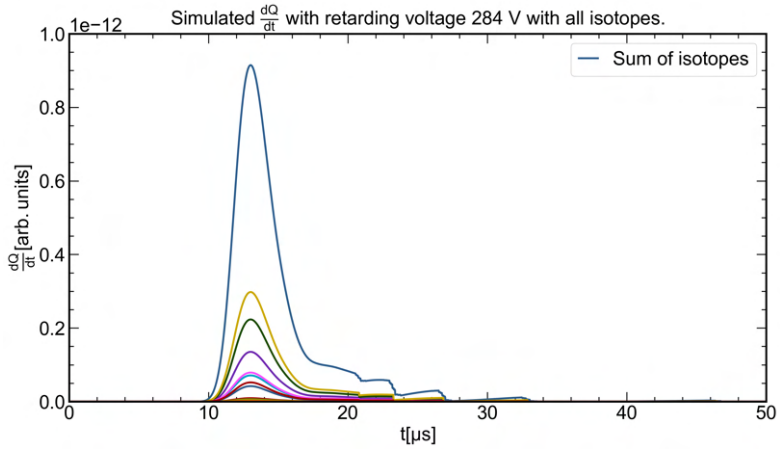

Figure 4.4.: Simulated $\frac{\mathrm{d}Q}{\mathrm{d}t}$ at 284 V with isotopes, each trace (except the sum of isotopes, shown in blue) corresponds to an individual isotope, the height of the traces is weighted by the abundance of the corresponding isotope. Steps in $\frac{\mathrm{d}Q}{\mathrm{d}t}$ correspond to additional charge states, which contribute for different isotopes at slightly different times.

4.6. Noise

To model experimental noise in our forward simulations, experimental time-of-flight traces have been studied. The mean standard deviation has been calculated for 60 retarding voltages by comparing all 100 shots for a certain voltage, for a certain observation angle. The photo-electron peak has been excluded for these calculations by demanding a minimum ToF of 2 us, which for a lenght of flight of 1 m corresponding to a kinetic energy of roughly 150 keV, well above the maximum energy of (significant) ion current.

The mean standard deviation decreases only between 2 and 10 %, while the ion current goes from maximum to completely blocked between 0 to 1000 V. The fact that the standard deviation remains roughly the same indicates that the difference between shots is mainly due to noise on the experimental equipment and/or thermal fluctuations and not due to difference between individual ion currents. This gives the motivation to apply a white noise in the simulations. This is done by adding a randomly chosen number from a normal distribution, with a mean of 0 and a standard deviation that is given by $\frac{\frac{dQ}{dt}_{peak}(U=0\,\mathrm{V})}{\mathrm{SNR}\sqrt{S_{\mathrm{shots}}}}$.

SNR is the signal to noise ratio, which here is defined as the ratio between the peak of the signal at zero retarding potential to the standard deviation of the zero retarding trace. The term $\sqrt{S_{\mathrm{shots}}}$ is included to make the simulations less computationally expensive. Instead of simulating for instance 100 shots, the effect of taking the mean value of 100 shots is immediately implemented. Taking the mean of S_{shots} reduces the error by a factor of $\sqrt{S_{\mathrm{shots}}}$.

Experimental values of SNR have been calculated, which range between roughly 30 and 90. To cover, and include these extrema, two values are investigated in our forward simulations, namely 25 and 100, additionally a value of SNR 400 is studied. This SNR value is included to study the behaviour at improved SNRs.

4.7. U_{ret} spacing

Originally, in experimental measurements the retarding voltage spacing was simply linear. For instance, from 1 to 100 V in 100 steps would yield a spacing shown in the 'Standard' column of table 4.1. Two alternative retarding voltage spacings have been considered namely logarithmic and *custom* spacing. The latter is explained below. Both methods ensure increased sampling at lower energies, this done to increase the sampling in the relevant energy range.

$\frac{U_{\mathrm{ret}}}{U_{\mathrm{ret,max}}}$	Standard [V]	Custom [V]	NU_{ret} Standard/Custom
0-25%	1, 2, ..., 24, 25	1, 1.5, ..., 24.5, 25	25/50
25-50%	26, 27, ..., 49,50	26, 27, ..., 49, 50	25/25
50-100%	51, 52, ..., 99, 100	51, 53, ..., 98, 100	50/25

Table 4.1.: Example of a standard versus *custom* retarding voltage spacing, with $\mathrm{U_{ret,max}} = 100\,\mathrm{V}$ and 100 retarding voltage steps. The custom spacing doubles the sampling rate for the bottom 25 %, keeps the rate the same for the subsequent 25 % and halves it for the remaining 50 %. The number of retarding voltage steps in a certain range are compared in the rightmost column.

For the custom $\mathrm{U_{ret}}$ spacing the sampling rate is doubled for the lowest 25%, kept the same for the the second 25% and is halved for the remaining 50% of the retarding voltage range. To illustrate the custom spacing, table shows 4.1 an example, with a maximum retarding voltage of 100 V and 100 retarding voltage steps.[1]

For all simulations the lowest retarding voltage is 15 V, which is similar to the lowest experimentally possible voltage of roughly 12 V. The highest retarding voltage is 2000 V. In total 60 retarding voltages are examined.

4.8. Realistic simulation

All earlier discussed parameters are probed independently to quantify their relative contributions. To examine a combination of these systematic effects, a 'realistic simulation' is also performed. This is a simulation, with isotopes, a SNR of 100 which is similar to experimentally observed SNR at low angles, an energy resolution FWHM of 1.1% and a increased transmission with a width of 5%. The last two values corresponds to the experimentally measured values of the Kimball FC73-A. The retarding voltage spacing is linear, with 60 points, ranging 15 to 2000 V.

4.9. Charge-state-resolved recovered energy

To quantitatively compare the effect of the use of different simulation parameters, charge-state-resolved and total recovered energies are calculated. As the input spectra and thus input energies are known, a comparison between input and recovered energy can be made to investigate the effect of the included effects.

These recovered energies are benchmarked in the following Chapter 5 against the idealized simulation, to give a measure of the relative contribution of the simulation parameter and the inherent energy deviations caused by the analysis method.

[1] This example is chosen to illustrate the custom spacing, the values chosen do not correspond to experimental values.

5. Results: Forward simulations

In this chapter the effect of different simulation parameters is investigated. To isolate each specific effect a standard idealized simulation is performed, from which only one parameter is changed. The standard simulation parameters are: a simulated scope time resolution of 20 ns, 60 linearly spaced retarding voltages, ranging from 15 to 2000 V, no noise, a single isotope mass, no sub-binning, constant transmission function and step-like energy resolution.

First, the results of four potential errors introduced in Chapter 4 are presented, after which three potential measurement improvements are investigated. These potential measurement improvements are: an increase in number of retarding voltages, alternative retarding voltage spacings and the use of sub-binning.

For all simulations charge-state-resolved spectra and energy are presented. The total energy is also presented alongside the charge-state-resolved energies. All energies are normalized by the input energies such that a recovered energy of 100 % means a perfect reconstruction, lower than 100 % means that the reconstruction underestimates energy and a recovered energy higher than 100 % corresponds to an overestimation. A black dashed line is included in all charge-state-resolved energy plots as a visual aid, if the recovered energy is closer to this line than the ideal simulation, the reconstruction is better. It follows that if the recovered energy is further away than the ideal simulation, the reconstruction is worsened by the simulation parameter.

The $\frac{\mathrm{d}Q}{\mathrm{d}t}$ trace shown in Figure 4.3 is an idealized simulation, where no measurement systematic effects have been included. Analysis of this idealized simulation yields Figure 5.1. The coloured lines are the Bottom-Up output and the black dotted lines are the input spectra. Broadening of spectra and peak height reduction can be observed (in the $z = 1$ spectrum for instance).

5.1. Energy resolution function

The recovered spectra obtained with a non step-like energy resolution are altered very minutely. The only difference is a very low, hardly visibly Sn^{2+} high-energy tail from roughly 2 to 3 keV. Although the number of ions assigned here is small, the increase in energy is significant. In Figure 5.2a the output spectra with an energy resolution FWHM of 1.1 % is shown, Figure 5.2b shows the same for a energy resolution FWHM of 2 %.

Figure 5.3, shows the charge-state-resolved normalized recovered energy, for different energy resolutions. The recovered energy is nearly unchanged for charge states 3, 4, 5 and 6. Sn^{1+}, Sn^{2+} and Sn^{7+} are more strongly impacted. A worse energy resolution leads to an increase in recovered energy for the first two, for

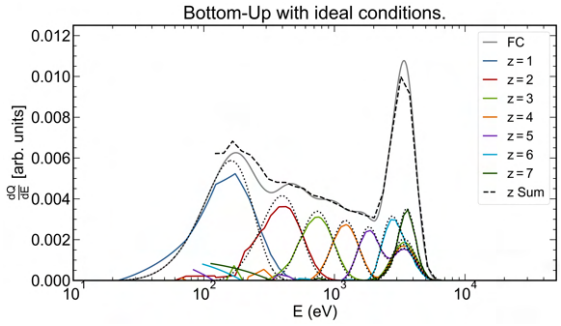

Figure 5.1.: Standard forward simulation result with idealized conditions, perfect step-like energy resolution, flat transmission, single isotope, no noise. 60 retarding voltage steps, linearly spaced between 15 to 2000 V.

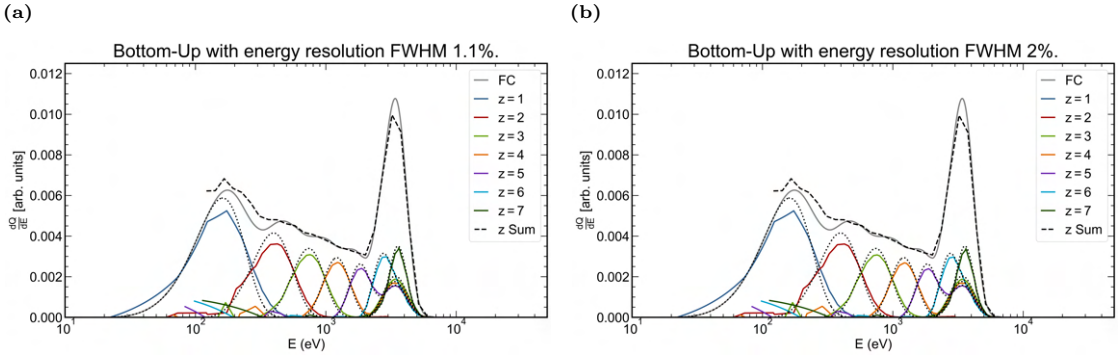

Figure 5.2.: Forward simulations with an energy resolution function modeled as a Gaussian cumulative distribution function with a FWHM of 1.1 % (a) and 2 % (b). In both cases a artificial, low current high-energy Sn^{2+} tail is present at energies between 2 to 3 keV

the last the recovered energy is decreased. To understand this, consider Section 3.2.1. Ions that from our prior assumptions can not pass, do pass and are measured with a non-perfect energy resolution. As the resolution worsens, an increasing amount of Sn^{2+} ions end up in the $\frac{dQ_{n=1}}{dE}$ spectrum for instance. This energy resolution contamination leads to an artificial increase in recovered (highly energetic) Sn^{1+} ions and thus total Sn^{1+} kinetic energy. Similarly, each cumulative spectrum receives an increasing number of ions of one (or more) charge states 'too high' based on the assumption.

The relatively large overestimation in recovered energy for Sn^{2+} of roughly 15 % is due to the fact that the secondary peak of Sn^{3+} is located at energies an order of magnitude larger than the Sn^{2+} peak. The Sn^{3+} ions incorrectly assigned to Sn^{2+} lead to a increase of roughly 11 to 13 %pt in recovered energy of Sn^{2+}, when compared to the idealized simulation. The increase in corresponding recovered ion number is 'only' 0.5 % and 1 % for a FWHM of 1.1 % and 2 % respectively. This indicates that the increase in recovered energy is due to the high energy of a relatively small number of misplaced Sn^{3+} ions.

Excluding the secondary Sn^{3+} peak in the simulation decreases the deviation between input and recovered energy from 12 to 15 % to roughly 3 %. This is in line with the reasoning that the relatively large increase in energy is due to the secondary peak being located in a higher energy range.

In the case of $\frac{dQ_{n=7}}{dE}$, there is no higher charge state to contaminate the spectrum. A contaminated and thus artificially increased $\frac{dQ_{n=6}}{dE}$ is subtracted from a regular $\frac{dQ_{n=7}}{dE}$ spectrum, leading to an underestimation in ion number in $\frac{dQ_{z=7}}{dE}$, and thus energy carried by Sn^{7+} ions.

For the remaining cumulative spectra (3-6), energy resolution contamination leads to a negligible effect on recovered energy. This is perhaps due to the fact that the contamination of each cumulative spectrum is approximately compensated by the subtraction of the preceding contaminated spectrum. In addition to this, the highest energy ions of these charge states are located at the same energies, thus energy resolution contamination does not increase the average or maximum energy of ions of a charge state significantly. The total recovered energy for both energy resolutions is nearly unchanged compared to the ideal simulation.

5.2. Isotopes

Figure 5.4 shows a comparison between the use of a single isotope (with abundance weighted mass of tin) and all isotopes in forward simulations. The inclusion of isotopes has a minute effect on the visual appearance of the spectra, similar to the energy resolution simulations. A low current Sn^{2+} high-energy tail is present around 2 and 3 keV.

Figure 5.5 shows the charge-state-resolved normalized recovered energy, for two simulations. The first simulation does not consider isotopes while the second includes all individual tin ions for time of flight calculations. A significant increase in recovered energy is observed for Sn^{2+}, which is caused by the

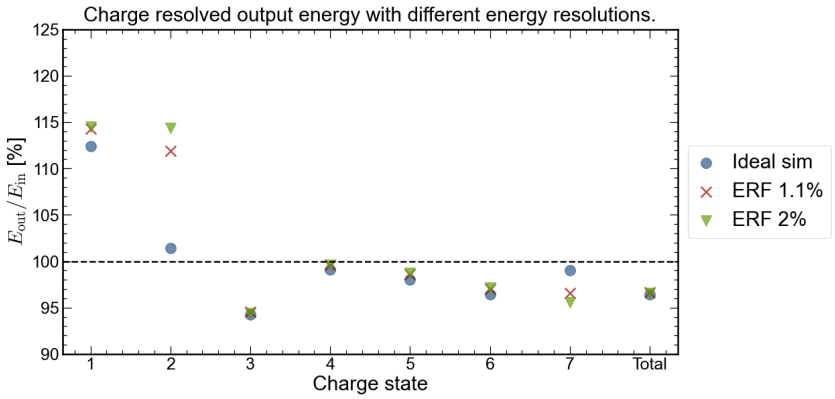

Figure 5.3.: Normalized charge-state-resolved recovered energy for different energy resolutions. For charge states Sn^{1+}, Sn^{2+} and Sn^{7+} the recovered energy is altered significantly compared to the ideal simulation. The energy increases for Sn^{1+} and Sn^{2+} with an increase in FWHM of the energy resolution function. The recovered energy decreases for Sn^{7+}. Total energy is nearly unaffected compared to the ideal simulation.

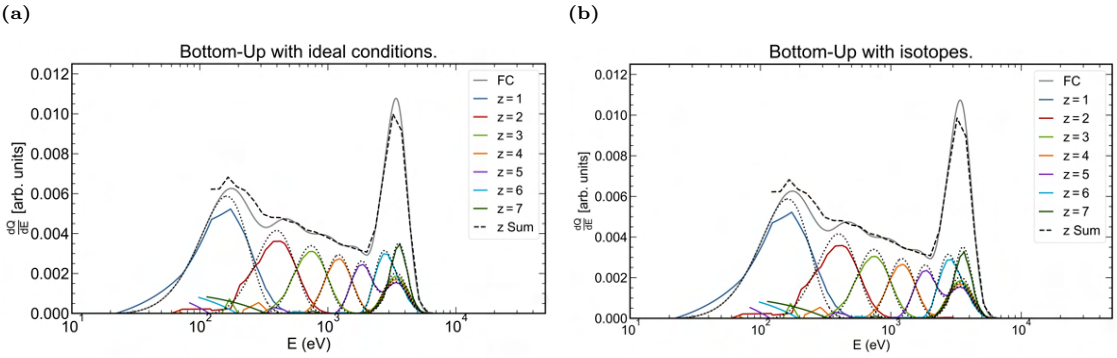

Figure 5.4.: Comparison of forward simulations with a single isotope of with the weighted average mass of tin (a) and all individual isotopes, weighted by their relative abundance (b).

high-energy secondary peak of Sn^{3+}. Heavy Sn^{3+} ions arrive at time-of-flights which correspond to the second energy bin and are thus assigned to Sn^{2+}. When the secondary Sn^{3+} peak is not included in simulations the large increase in recovered Sn^{2+} energy nearly disappears completely. For the remaining charge states only a small deviation from the idealized simulation is observed.

For the Sn^{7+}, a decrease in recovered ion energy and number is observed. The cause of this is the same as the decreased recovered energy for the energy resolution, discussed above.

5.3. Potential dependent transmission function

Figure 5.6 shows the result of forward simulations with a increased transmission. All spectra are artificially increased by increased transmission and more so when the width is increased. This increase is caused by an increasing fraction of ion current being overestimated. Figure 5.7 shows the charge-state-resolved normalized recovered energy for a potential dependent transmission width of 5 and 10%. The charge-state-resolved recovered energy increases with increased transmission, this can be understood by the fact that a larger fraction of the current enclosed in the bin is overestimated. This increased transmission leads to an overestimation in ion number and subsequently energy. The 5 % width corresponds the experimentally

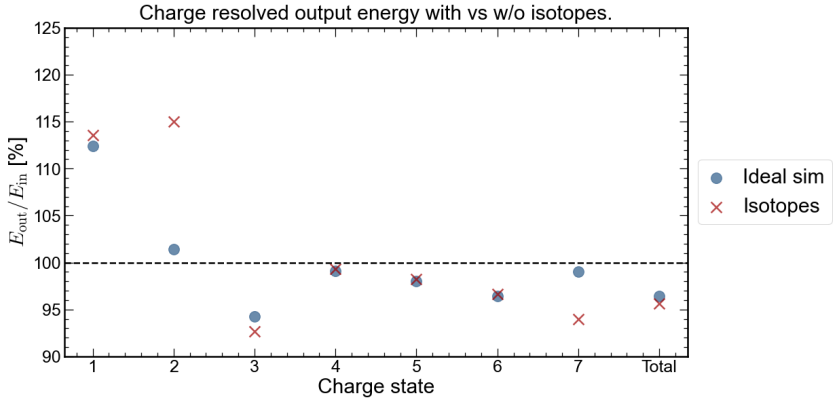

Figure 5.5.: Normalized charge-state-resolved energy for ideal simulation (single isotope) and a simulation including all isotope masses, weighted by natural abundance. Heavy isotopes 'arrive late', leading to isotope contamination of the previous bin. Recovered energy increases for Sn^{1+} and Sn^{2+} due to contamination. The recovered energy of Sn^{3+} and Sn^{7+} is decreased. Total recovered energy is slightly decreased.

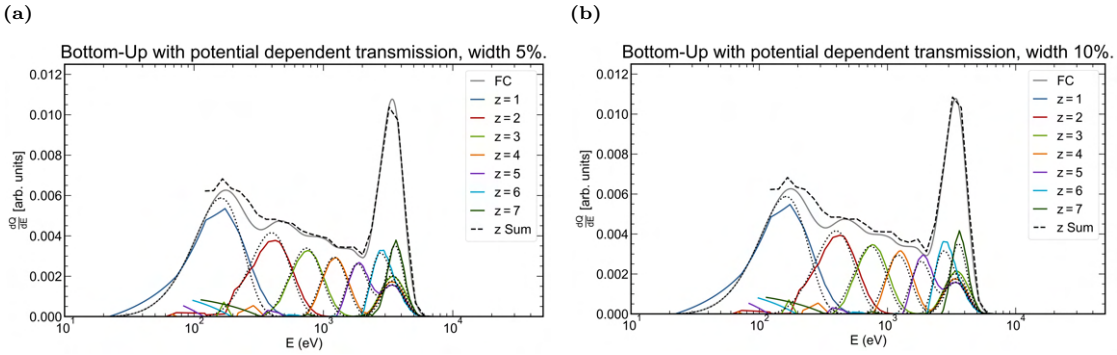

Figure 5.6.: Comparison of forward simulations with potential dependent transmission of different widths with a ideal simulation. The charge-state-resolved spectra have an increased height for a larger width of increased transmission.

observed increased transmission in the RFAs used. For this simulation an increase of 5 %pt of total energy from the ideal case is observed.

5.4. Noise

Figure 5.8 shows a comparison between three simulations with noise, with a signal to noise ratio (SNR) of 25, 100 and 400. A large increase in assigned Sn^{1+} ion current can be observed, which is most pronounced at the low value of SNR. Figure 5.9 shows the charge-state-resolved normalized recovered energy, for different values of SNR. This is shown on logarithmic scale to include the high values of normalized recovered energy at Sn^{1+}. The recovered energy of the Sn^{1+}, becomes roughly 200 % and 500 % of the input energy for a SNR of 100 and 25 respectively. A decrease in Sn^{2+} energy of roughly 20 %pt can be observed for the SNR 25 case, which corresponds to the reduction in height of the Sn^{2+} spectrum in Figure 5.8a. The reduction of the Sn^{2+} spectrum is due to the artificially increased spectrum of Sn^{1+}.

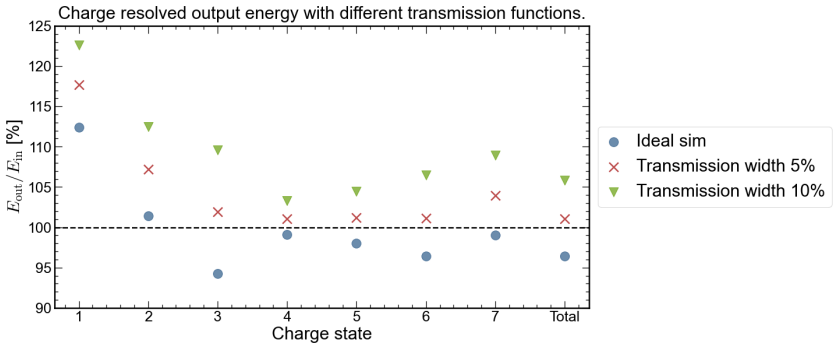

Figure 5.7.: Normalized charge-state-resolved recovered energy for different widths of potential dependent increased transmissions. As the width of increased transmission grows, the ion current is overestimated increasingly. This leads to an overestimation in the assigned ion number and energy.

The artificially increased Sn^{1+} spectrum is subtracted from the cumulative $\frac{dQ_{n=2}}{dE}$ spectrum, causing the $\frac{dQ_{z=2}}{dE}$ to be reduced in height.

The strong increase in Sn^{1+} (when compared to the remaining charge states) due to noise is due to two effects. First, following Sheil et al. [23], the average charge state of ions ($\bar{z}$) emitted from LPPs, is proportional to their kinetic energy, $\bar{z} \propto E^{0.4}$ thus the spectra of lower charge states peak at a lower energy than higher charge states. Additionally, assuming white noise in ToF traces, the energy domain noise level is proportional to

$$\text{Noise} \propto \frac{dt}{dE} \propto E^{-\frac{3}{2}}, \tag{5.1}$$

due to transformation from time to energy domain current [21]. Lower charge state thus have less kinetic energy on average than higher charge states and noise affects energy domain current at low kinetic energy more strongly. Putting these two facts together we can see that noise affects lower charge states more strongly.

Secondarily, subsequent cumuative spectra are subtracted from each other, meaning that the noise floor is subtracted for all charge state higher than 1. Total recovered energy is nearly unchanged in all SNR cases as noise mainly leads to an increase in ion assignment at low energies.

5.5. Number of retarding voltage steps (NU_{ret})

Two alternative number of retarding voltages (NU_{ret}) are studied, half the standard number and double, i.e. $NU_{ret} = 30$ and 120. Each charge-state-resolved spectrum can get at most NU_{ret} points assigned to it. Increasing NU_{ret} should lead to less jagged spectra, which might lead to an improvement in reconstruction.

Figure 5.10a shows the outcome of the simulation with 30 retarding voltages, the charge-state-resolved spectra are more jagged than with 60 retarding voltages. Figure 5.10b shows the outcome of the simulation with 120 retarding voltages, the charge-state-resolved spectra become more smoothed out. The spectra resemble the input more closely when compared with the 60 retarding voltage simulation. However the effect of binning, which is a reduction of peak height and broadening of spectra, cannot be remedied by including more retarding voltages.

Figure 5.11 shows the calculated energies. Even though the shape of the spectra seem to match the input better no clear improvement in charge-state-resolved or total energy is observed with a higher number of retarding voltages.

However, an increase of roughly 2 percentage points in recovered energy can be observed for Sn^{2+} in the 30 retarding voltage case. This increase seems to be related to the missed peak of the first cumulative spectrum, the 'missed' current gets assigned to Sn^{2+}, increasing the assigned ion number and energy. For all values of NU_{ret} studied, an overestimation in energy of Sn^{1+} of roughly 12 to 13 % is observed which is due to spectra broadening. Spectra broadening can not be mitigated by the number of retarding voltages.

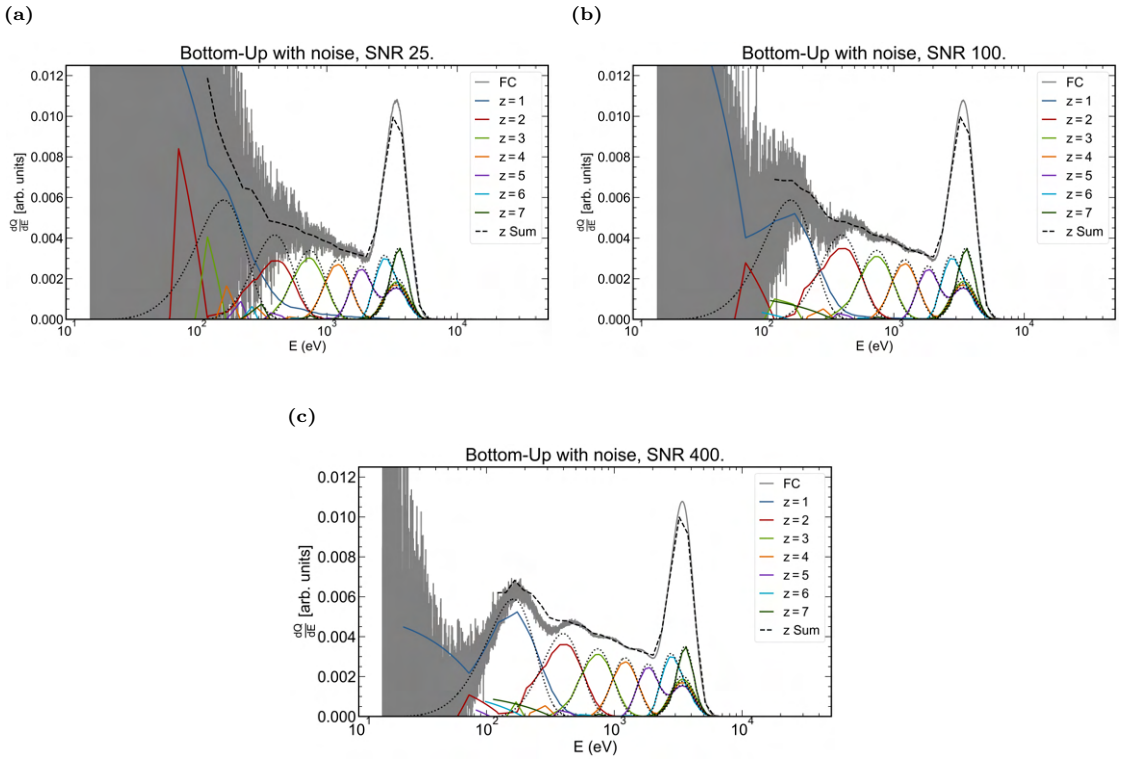

Figure 5.8.: Comparison of forward simulations with noise with three different signal to noise ratios, namely 25, 100 and 400 in (a), (b) and (c) respectively.

5.6. Retarding voltage spacing

Figure 5.12a shows the result of the forward simulation using a logarithmic retarding voltage spacing. Using logarithmically spaced steps strongly increases sampling rate at low retarding voltages (and thus low energies). This increased sampling can be seen by looking at the obtained $z = 1$ spectrum for instance. As more low retarding voltages are included, the spectrum becomes less jagged.

Figure 5.12b shows the result of the forward simulation using the custom retarding voltage spacing discussed in Section 4.7. The increased sampling at lower retarding voltages leads to less jagged spectra.

Figure 5.13 shows the charge-state-resolved normalized recovered energy, for simulations performed with a linear, logarithmic and *custom* retarding voltage spacing. No clear improvement in recovered energy can be observed using either alternative method.

5.7. Sub-binning

Figure 5.14 shows the use of 2 and 3 sub-bins. When compared to the simulation without sub-binning in Figure 5.1, the recovered low charge state spectra match the input better. The reconstruction is however worsened at higher charge states, which might be related to the sampling rate in ToF. The amount of time-steps between the extrema of a sub-bin energies decrease as the number of sub-bins increases. This can lead to numerical instabilities as numerical (trapezoidal) integration is employed to obtain the mean current. A simulation with a scope time-step of 2 ns is performed to investigate the cause of the worsened reconstruction. Figure 5.15 shows that the recovered high charge state spectra improve with this time resolution, indicating that the decrease in reconstruction observed in Figure 5.14 is indeed caused by numerical instabilities caused by ToF sampling rate of 20 ns being too coarse.

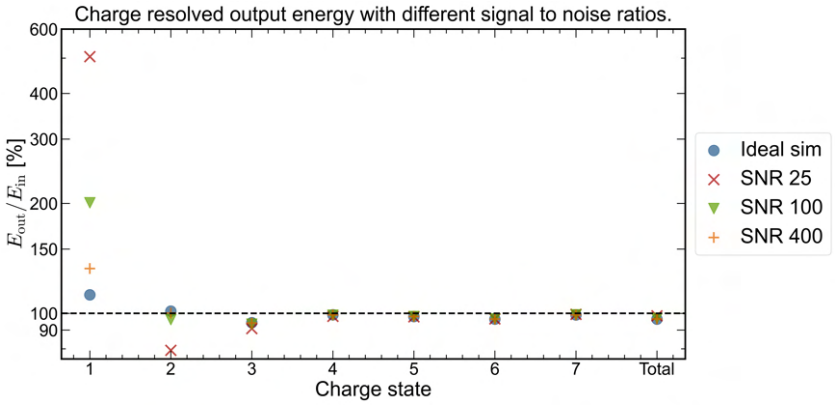

Figure 5.9.: Normalized charge-state-resolved recovered energy for different values of signal to noise ratio (SNR). For increasing values of SNR, the energy assigned to Sn^{1+} increases significantly.

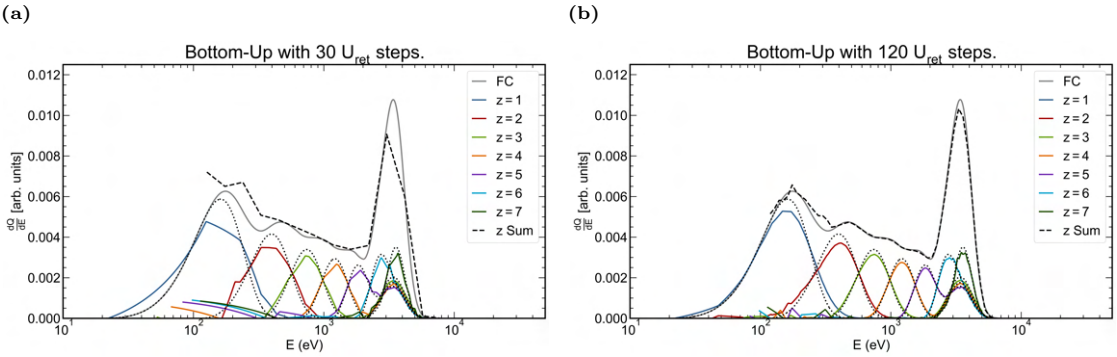

Figure 5.10.: Forward simulations with different number of retarding voltage steps, half and double the standard of 60.

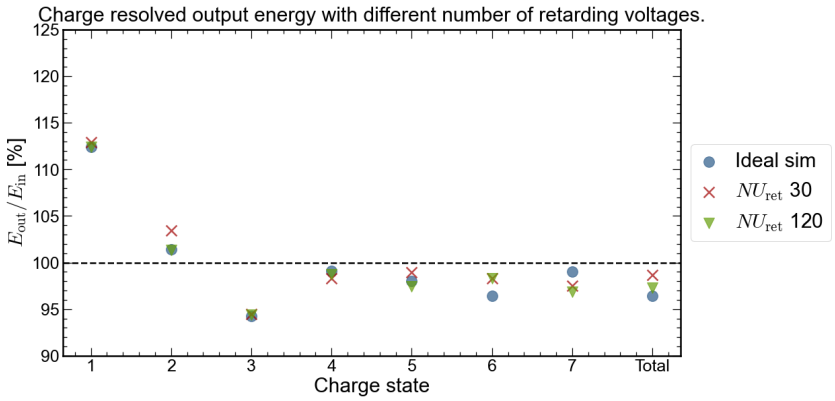

Figure 5.11.: Normalized recovered charge-state-resolved energy for different number of retarding voltages. The recovered energy does not deviate meaningfully when doubling or halving the amount of retarding voltages. No clear trend is visible.

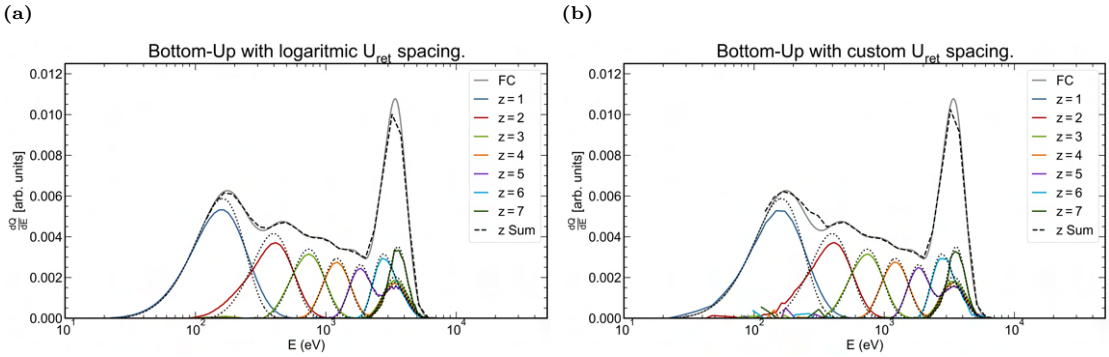

Figure 5.12.: Forward simulations with different retarding voltage spacing. Logarithmic spacing has been used in (a) and the custom spacing described in Section 4.7 is used for (b).

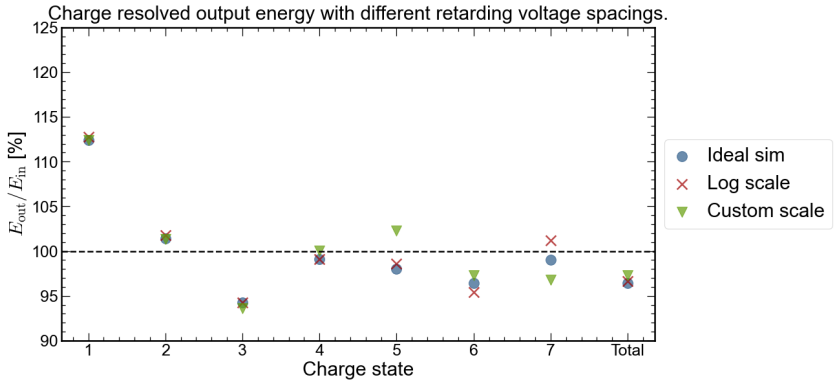

Figure 5.13.: Normalized charge-state-resolved recovered energy for linear, logarithmic and *custom* U_{ret} spacing. No clear effect of retarding voltage spacing on recovered energy can be observed.

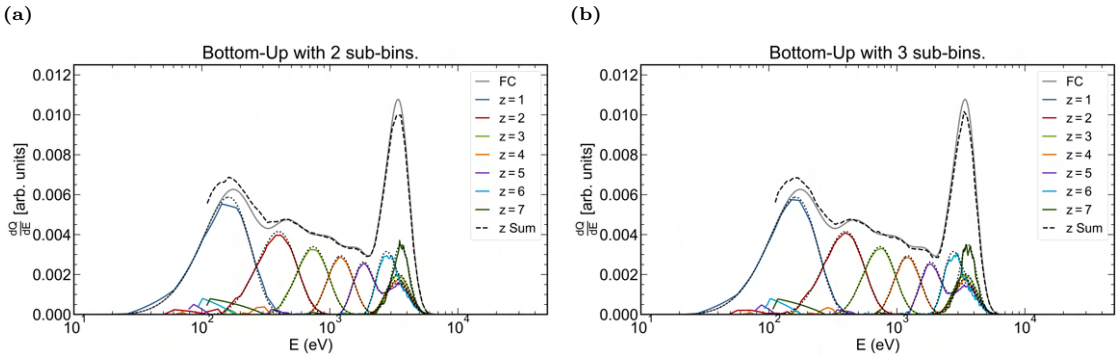

Figure 5.14.: Comparison of forward simulations with 2 and 3 sub-bins in (a) and (b) respectively. The spectra of lowest charge states match the input spectra better with the use of sub-bins. At the higher charge states the reconstruction becomes worse due to numerical instability.

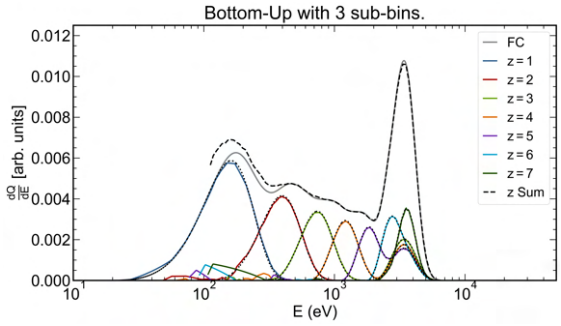

Figure 5.15.: Forward simulation using 3 sub-bins, with a time resolution of 2 ns. All reconstructed spectra closely resemble the input.

Figure 5.16a shows the normalized recovered charge-state-resolved energy for different number of sub-bins for a time resolution of 20 ns. For the first three charge states the use of sub-binning leads to the deviation between recovered energy and input decreasing. An improved reconstruction is obtained for these charge states with the use of sub-bins. However, from Sn^{4+} onwards the use of sub-bins leads to a worse recovered energy. This is related to the numerical instability introduced by the ToF sampling rate, also observed in Figure 5.14. When a time resolution of 2 ns is employed the issue of numerical instability is mitigated. Using this finer ToF sampling of 2 ns the reconstructed energies improve with an increase in number of sub-bins from none to three, which is shown in Figure 5.16b. The use of a ToF resolution of 2 ns leads to both charge-state-resolved and total energy being improved by sub-binning. The total recovered energy is 99.5 % of the input for both sub-binning cases, compared to 98 % for conventional binning. The use of sub-binning is most beneficial at low charge states. This is in line with the fact that spectra broadening and peak height reduction are inversely proportional to bin number (see Equation 3.22 and 3.23). The use of the fine ToF resolution is most beneficial at higher charge states due to numerical instability at high energy. It can be deduced from Figure 5.16 that numerical instability negatively affects the reconstruction from charge state $z = 4$ onwards even in the 'ideal' case. The ToF resolution of 20 ns is not only insufficient for sub-binning, even conventional binning is negatively affected by this resolution.

5.8. Realistic simulation

In the foregoing sections, a collection of individual systematic effects, and potential measurement and analysis improvements were studied by simulation. Sub-binning is the most promising of the improvements, however in the simulations, numerical instabilities occur for a time resolution of 20 ns. Using a time resolution of 2 ns leads to a improvement in recovered ion energy and number for all charge states.

To investigate the viability of sub-binning on experimental data, additional 'realistic simulations' are performed. These simulations are based on the idealized simulations, with the inclusion of all systematic effects studied with values close to those experimentally observed. An energy resolution FWHM of 1.1 %, isotopes included, increased transmission width of 5 %, noise with a SNR of 100. Furthermore, a time resolution of 2 ns is used to prevent sensitivity to numerical instability and different numbers of sub-bins are employed.

Figure 5.17 shows the result of the realistic simulations for different number of sub-bins used on the realistic simulations. At first glance including sub-bins seem to lead to 'noisier' recovered spectra. However, after further inspection a sawtooth pattern is observed, rather than random noise. Analysis shows that this pattern is not due to noise, but to the fact that three of the experimental systematic effects affect the current around the edges of the energy bins more strongly. Isotopes, energy resolution and transmission lead to the current at the bin edges being altered. This means that when sub-binning is used, that the extrema sub-bins will be most affected by systematic effects, leading to an increased uncertainty about charge state in these energy regions. This can lead to an over/underestimation of ion current in these sub-bins. This is the motivation for excluding the extrema sub-bins to prevent this uncertainty, which is further discussed below.

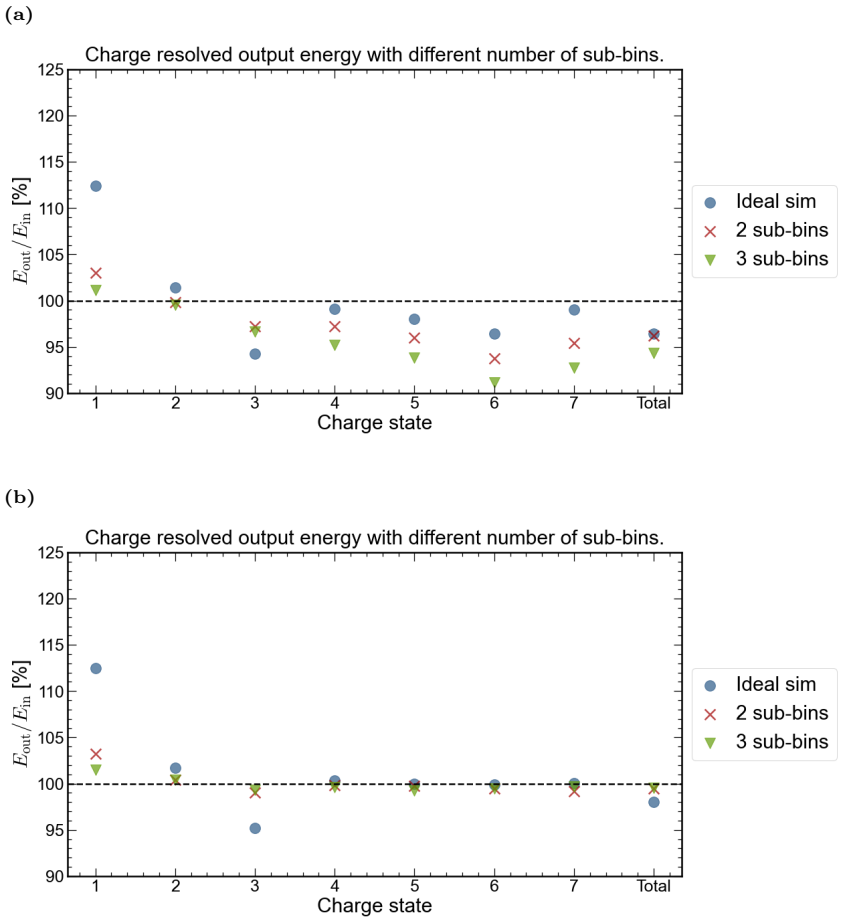

Figure 5.16.: Normalized recovered energy employing no, 2 and 3 sub-bins. Time resolution of 20 ns and 2 ns used in (a) and (b) respectively. In (a) the deviation between input and recovered energy decreases for the charge states until Sn^{3+}, indicating an improvement in the spectrum reconstruction. For the higher charge states the recovered energy deviates from the input with an increase in sub-bins. This is caused by numerical instability caused by the ToF sampling.

Figure 5.18 shows the charge-state-resolved normalized recovered energy, with all experimental systematic effects included. The use of sub-bins improves the recovered energy for Sn^{1+} slightly. For Sn^{2+} and Sn^{3+} the recovered energy is overestimated compared to no sub-binning. For the remaining charge states no clear trend is visible, indicating that the reconstruction does not improve or worsen significantly. The total energy is best when no sub-binning is employed however. The total energy reconstruction is close to 100 % in all cases.

5.8.1. Excluding extrema sub-bins

Systematic effects such as isotope spread, energy resolution and increased transmission, have a (larger) effect at the extrema of an energy bin than in the centre. To minimize the sensitivity to these effects we can exclude the extrema sub-bins from our analysis. Excluding 2 extrema sub-bins is only possible from 3

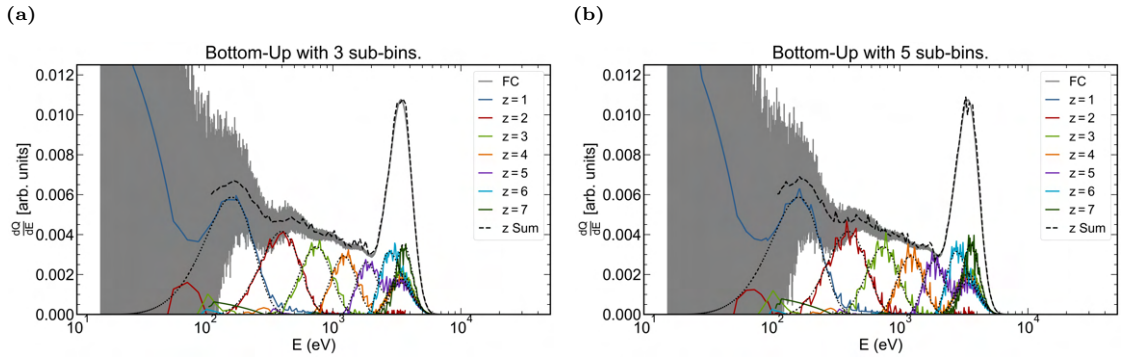

Figure 5.17.: Realistic simulation analyzed using different number of sub-bins, 3 and 5 sub-bins have been used in (a) and (b) respectively. As the number of sub-bins is increased, a sawtooth pattern becomes visible. This pattern is explained by the fact that the sub-bins at the extrema of a bin are more affected by certain systematic effects. These effects lead to an over/underestimation of current in these sub-bins, leading to the observed pattern.

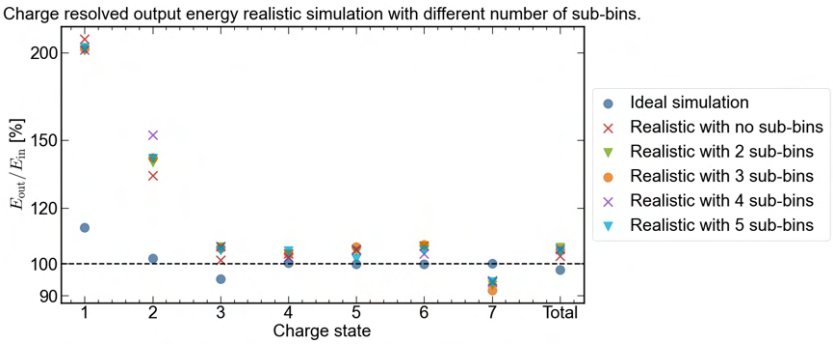

Figure 5.18.: Recovered energy for realistic simulations with different number of sub-bins. The use of sub-bins does not lead to an improved recovered energy, the total energy is further overestimated in all sub-binning simulations, compared to the conventional binning simulation

sub-bins onwards, thus the use of 3, 4 and 5 sub-bins is investigated. This leads to the exclusion of $\frac{2}{3}$, $\frac{1}{2}$ and $\frac{2}{5}$ of our collected data respectively.

Figure 5.19 shows three examples of the recovered spectra using this method, when compared to 5.17 the sawtooth pattern is reduced. At higher charge states the pattern does appear when using an increasing number of sub-bins, this is explained by the fact that the systematic effects affect a larger fraction of the energy bin at these charge states. Fortunately, sub-binning is most beneficial at low bin numbers as the spectra broadening and peak reduction is inversely proportional to bin number.

Sub-binning proves beneficial in ideal simulations especially at low bin-numbers. Sub-binning leads to a sawtooth pattern in realistic simulations and exclusion of the extrema sub-bins reduces this pattern. The foregoing findings lead to the motivation for using custom number of sub-bins per bin and excluding extrema sub-bins. The custom sub-binning method uses 5 sub-bins for bin 1 through 4, 4 sub-bins for bin 5 and 3 sub-bins for bins above 5, the extrema sub-bins are excluded from analysis. This custom binning method has been implemented on our simulations, yielding Figure 5.19d, where the sawtooth pattern is nearly entirely mitigated, while reaping the benefit of sub-binning.

Calculating the normalized recovered charge resolved energies yields Figure 5.20a. It can be observed that excluding the extrema sub-bins leads to a recovered energy more in agreement with the input than employing no sub-binning for all charge states. The recovered energy is worsened by for Sn^{3+}, however the

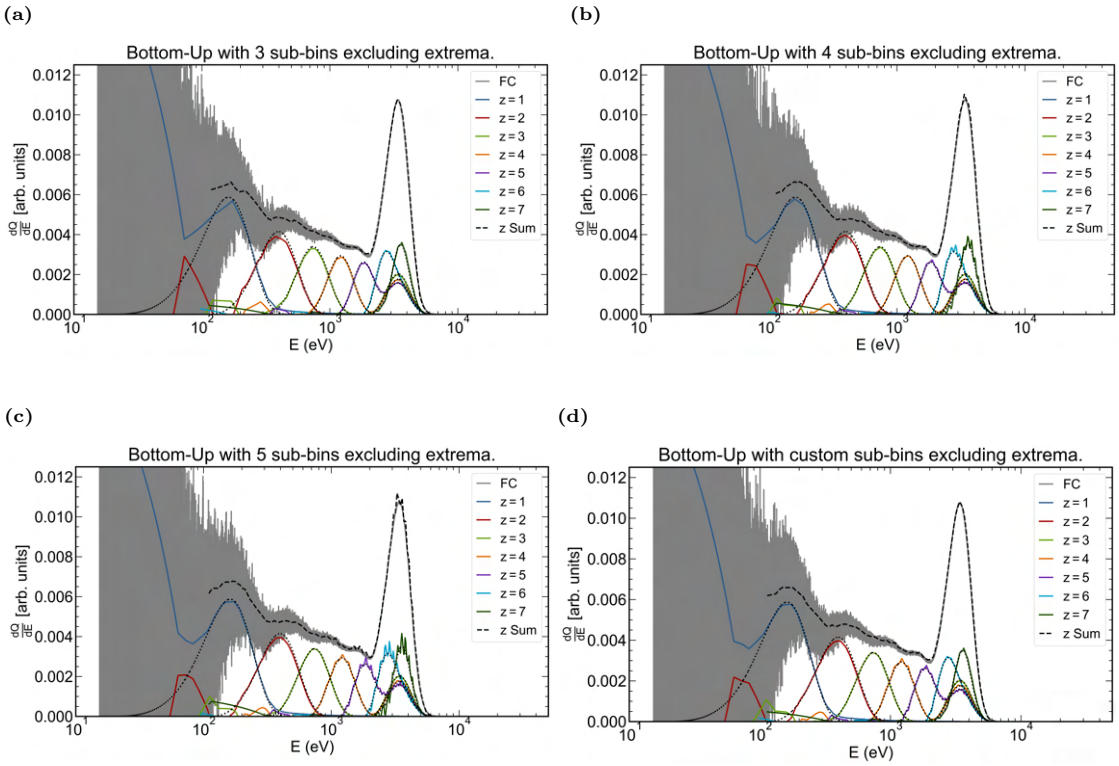

Figure 5.19.: Realistic simulations employing sub-binning, excluding the 2 extrema sub-bins. Subfigure (a), (b) and (c) show the use of 3, 4 and 5 sub-bins respectively. In general a reduction in sawtooth pattern is observed when excluding the extrema sub-bins, with a improved reconstruction of input spectra. For the higher charge states the sawtooth pattern does appear at 4 sub-bins (z = 6 & 7) and 5 sub-bins (z = 5, 6 & 7). A custom number of sub-bins is used in (d), yielding a good reconstruction, with a mitigated sawtooth pattern.

close match between input and recovered energy here seems fortuitous as the recovered energy deviates more from the input energy in the idealized simulation than the realistic simulation. The total energy is improved or unchanged when compared to conventional binning.

Finally, the normalized recovered energies employing custom number of sub-bins are compared to the use of no sub-binning in Figure 5.20b. The custom sub-binning method leads to an improvement in charge-state-resolved and total energy. The only exception to this improved reconstruction again is the third charge state, which is due to the fortuitous near perfect reconstruction with the conventional binning method.

Figure 5.21 shows the total recovered energies normalized by the input energies for the three simulations employing a time resolution of 2 ns. Those being an ideal simulation and two realistic simulations. The first realistic simulation makes use of conventional binning method and the second makes use of the custom binning method. The recovered total energy is improved by one percentage point for the custom sub-binning method when compared to the standard binning method. The recovered energy is very similar to the input for all three cases, a maximum deviation of 2.5 percentage points is observed when conventional binning is used, decreasing to a deviation of 1.5 %pt using custom sub-bins.

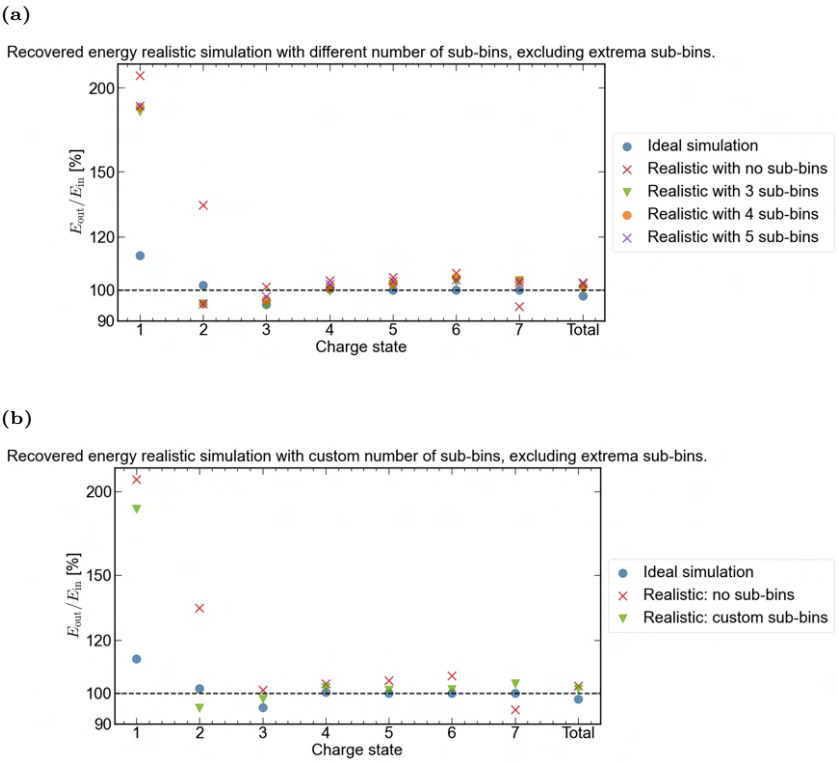

Figure 5.20.: Recovered energy employing exclusion of the extrema sub-bins, (a) shows the use of a consistent number of sub-bins for all different bins. Based on the observed sawtooth pattern a custom number of sub-bins is chosen that minimizes the pattern, the results of the use of this custom binning method are shown in (b).

5.9. Discussion of forward simulations

In this chapter the results of the forward simulations have been presented. These simulations provide insight into systematic effects which might affect the Bottom-Up output spectra and recovered figures therefrom. In particular, the effect on assigned ion number, energy and momentum have been studied.

The magnitude in ion number, energy and momentum deviation that has been reported, might not in general be exactly the same for experimental data. This is due to the fact that the input spectra have been chosen to resemble the low angle emission of a plasma driven with a 1 um laser on a droplet target. Plasmas driven at different laser wavelengths, spatial and temporal pulse shapes or intensities might display disparate emission of ions. Furthermore, the input spectra have been chosen to resemble those found by the Bottom-Up method of experimental data of 1 um laser driven plasmas, however the exact spectra are not known as their reconstruction is exactly the aim of the Bottom-Up analysis. Conclusions taken on the basis of the simulations performed then should be understood to give an indication about the magnitude of potential uncertainty due to experimental and analysis systematics, rather than precise statements about experimental deviations in all cases.

Keeping the foregoing in mind, the forward simulations show that a significant artificial increase in Sn^{1+} ion number, momentum and energy can occur due to noise. This increase is between 100 to 400 % in our simulations for values of signal to noise ratio corresponding to those found in experimental data. This percentage increase might not be representative for experimental measurements however, if a very minute number of Sn^{1+} are ejected from an LPP. For a minute emission the noise contribution will represent a larger fraction of the assigned Sn^{1+} current. The difference between actual and assigned ion number

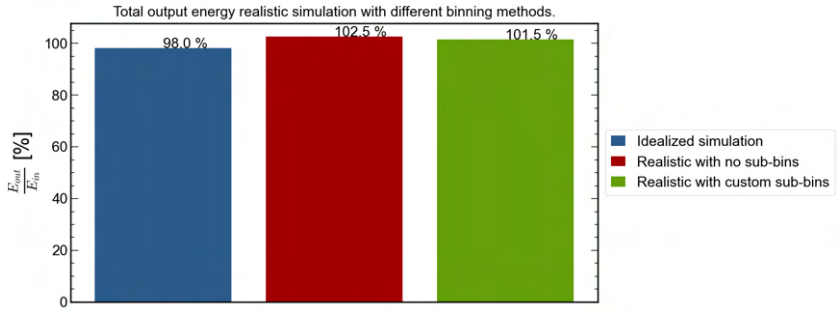

Figure 5.21.: Normalized total energy for one idealized and two realistic simulations. The realistic simulations have been analyzed using two alternative binning methods: no sub-binning and the use of a custom number of sub-bins, excluding the extrema.

would be a higher percentage in this case. If Sn^{1+} emission is high the reverse is true the overestimation of Sn^{1+} would represent a smaller percentage as the Sn^{1+} ion current signal is much larger than the noise. The total energy is hardly affected as the Sn^{1+} is at lower energies than the higher charge states.

The assigned ion energy for Sn^{2+} in our simulations increases significantly due to non-perfect energy resolution and inclusion of isotopes. Highly energetic Sn^{3+} are measured in the second energy bin in our simulations. The large increase in ion energy is explained by the fact that the Sn^{3+} spectrum extends to significantly higher energies and has a much higher ion number than Sn^{2+} spectrum. The increase in assigned Sn^{2+} would have been smaller if the secondary high-energy peak of Sn^{3+} had not been included or had been lower. The exact height, width, and position of the input spectra determines the magnitude of incorrectly assigned ions and therefore the magnitude of the deviation in recovered ion number, energy and momentum. More generally, if a charge state has an emission much smaller or at energies much smaller than one charge state higher, the ion number and energy might be significantly overestimated.

Sub-binning leads to an improved reconstruction for a idealized simulation with sufficiently fine time-of-flight resolution. More remarkably, a resolution of 20 ns leads to numerical instability even with conventional binning.

Moving away from the ideal simulation to a simulation including all systematic effects, sub-binning does not significantly improve the recovered energy. This is due to the fact that most of the systematic effects modify current, which affects the extrema of the bins more strongly. This leads to a sawtooth pattern on the charge-state-resolved spectra when sub-binning is employed.

Excluding sub-bins has been investigated to mitigate the sawtooth pattern. Using this alternative binning method mitigates the sawtooth pattern. The pattern does remain for higher charge states at increasing number of sub-bins. To reap the benefit of sub-binning at lower charge states while mitigating the sawtooth pattern at higher charge states, a custom number of sub-bins is assigned for each bin. This yields a closer match between input and output energy for all charge states, except for Sn^{3+}. The last fact seems to be due to a coincidental near-perfect reconstruction of Sn^{3+} energy when using no sub-bins.

Using a custom number of sub-bins with the addition of excluding the extrema sub-bins seems viable for experimental data to recover an improved reconstruction of output energy for all charge-states and a slight improvement of 1 %pt of the total energy. For most charge states however the energy deviation decreases by single digit percentage points as the recovered energies are already in very good agreement using conventional binning.

It was not possible to include all RFA effects into the forward simulations due to time constraints. The author believes that the most important effects have been included, however the change in time-of-flight due to drift or acceleration might merit further investigation (see Chapter 2 and Appendix A.2). Earlier work shows that this could introduce a significant systematic error in assigned energy of a small fraction of ions. Further research might be necessary to investigate the effect of drift/acceleration of ions on time-of-flight data and subsequently the uncertainty that this introduces in the Bottom-Up method. This would yield an even more comprehensive view of uncertainties introduced by our measuring method. It

might therefore be insightful to model this drift/acceleration by making use of electrostatic simulation software, such as *SIMION*, to obtain time-of-flight data.

The exact value of the simulated noise is different for each simulation including noise. This might introduce a dependence on the exact values of the noise on the results. Per simulated measurement, at least 10.000 noise points are assigned, thus it is unlikely that a (strong) bias is introduced. The recovered ion energies for the different signal to noise ratios are very reproducible despite this fact.

The transmission function was modeled by two constants, the value used depends on the ion energy, charge state and retarding potential. In reality the transmission function has a more complicated dependence and cannot simply be taken to be one of two constants. The transmission might also be influenced by the potential on the suppressor grid, especially if the magnitude of the suppressor grid is greater or equal to the retarding potential. Taking into consideration these facts might introduce further effects not captured in this work. Future research could make use of experimentally obtained transmission functions which might give a more accurate result of potential effects of transmission on reconstructed spectra and ion energy.

For most simulations performed with single systematic effects the total reconstructed energy is very similar to the ideal simulation only deviating single digit percentage points. The transmission function shows the largest effect, with an overestimation of 5 %pt for a transmission based on the Kimball FC-73A. Remarkably the deviation between input and recovered energy is larger for this single parameter, than the deviation in realistic simulations including all parameters. Evidently, the effect of the experimental systematics on energy partially cancel each other out.

6. Results: Experimental test

To validate the results found in the simulations, experimental tests have been performed. In these tests a 1 um laser has been used on a tin microdroplet target. Ion emission was recorded at a measurement angle of 30° with respect to the incoming laser. The maximal scope ToF resolution of 2 ns has been used to prevent sensitivity to numerical instability (see Chapter 5).

6.1. Maximum scope resolution

The experimental findings of increasing the scope sampling rate are presented here. The sampling rate is increased to make sub-binning (more) feasible with experimental data. To ensure minimal sensitivity to noise and numerical instability (see Section 5.7) each energy sub-bin should correspond to a few dozens of points at least. For these experimental tests the sampling rate of the scope is set at the maximum of 100.000 points for 200 µs, yielding a time resolution of 2 ns.

Two examples of sub-binning on experimental data are shown in Figure 6.1, with 2 and 5 sub-bins. A sawtooth pattern can be observed on the charge-state-resolved spectra, in agreement with the realistic simulations which display a similar sawtooth pattern when sub-binning. In simulations the pattern is mainly caused by the inclusion of isotopes and potential dependent transmission function. The measured current is modified by these effects, mainly at the extrema of a bin, which can lead to the mean current being increased or decreased in those sub-bins.

In the forward simulations, using sub-bins and the excluding the extrema sub-bins leads to a improved reconstruction with a reduction in sawtooth pattern. The sub-binning and exclusion analysis method is applied on experimental data to study if the sawtooth pattern on the experimental spectra can also be reduced.

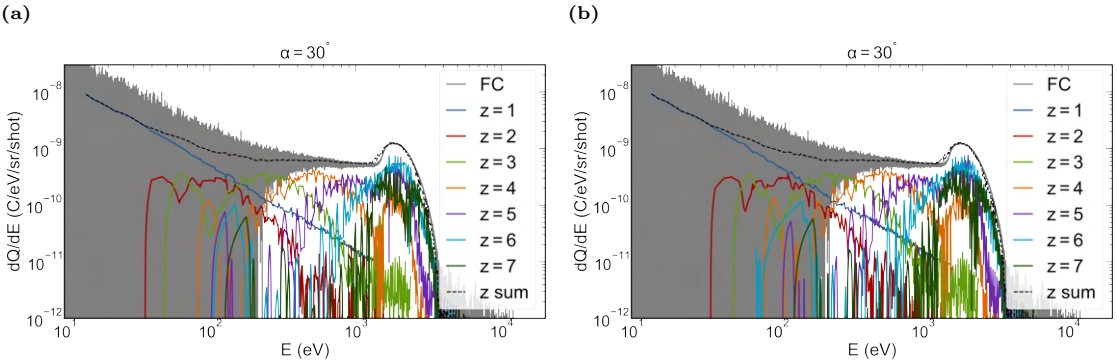

Figure 6.1.: Two examples of spectra obtained using the maximum scope resolution, with the addition of sub-binning. (a) shows the use of two sub-bins, (b) shows the use of five sub-bins.

6.1.1. Excluding extrema sub-bins

Figure 6.2a shows the use of five sub-bins and excluding the two extrema sub-bins. When compared to the spectra in Figure 6.1b (both use five sub-bins), a reduction of sawtooth pattern can be observed. This reduction is explained by the fact that contamination is mainly present at the edges of our energy bins, and thus the extrema sub-bins are most affected.

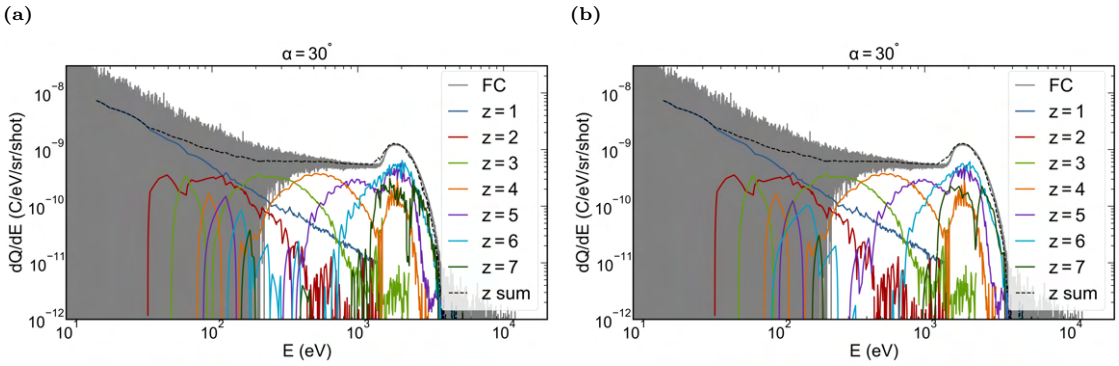

Figure 6.2.: Two examples of sub-binning with the exclusion of the two sub-bins at the extrema. (a) shows the use of five sub-bins for all bins, (b) shows the use of a custom number of sub-bins.

Based on observations from the realistic simulations, a custom number of sub-bins (see Section 5.8.1) might lead to an improved reconstruction for all charge-states. Figure 6.2b shows the use custom number of sub-bins. In all bins the two sub-bins at the bin extrema are excluded from analysis. The recovered spectra show a reduction in sawtooth pattern in agreement with the forward simulations.

The effect of the excluding sub-bins on recovered energy, ion number and momentum is also studied. Although the precise value of these figures is not known, we can examine the sensitivity of the recovered values to the use of different binning methods. Three alternative binning methods are studied, the use of 5 sub-bins, the use of the custom number of sub-bins and the use of 3 sub-bins. For the last two binning methods the exclusion of extrema sub-bins has also been used. Figure 6.3a shows the charge-state-resolved recovered energy. The recovered ion numbers are also shown in Figure 6.3b.

Figure 6.3a shows the charge-state-resolved ion energy for different discussed methods. The charge-state-resolved ion number (Figure 6.3b) and momentum show a similar weak sensitivity to the different binning methods considered. It follows that the total recovered ion energy (shown in Figure 6.5), number and momentum also have a weak sensitivity to the specific binning methods. For all alternative binning methods considered, the percentage change on the total figures is roughly 1 % when compared to conventional binning. The largest deviation is a reduction in total recovered ion number of 1.5 % when using custom sub-bins when compared to conventional binning. Recovered momentum is nearly unchanged and recovered total kinetic energy increased by 1.1 %.

6.1.2. Downsampling time-of-flight resolution

The forward simulations show that a ToF resolution of 20 ns is insufficient as it can lead to numerical instability. The numerical instability can lead to an underestimation in ion current and subsequently calculated ion number, energy and momentum. Numerical instability mainly affects ion current at high energies and more so when sub-binning is employed.

In this section the experimental data used for in the maximum resolution test is compared. The same data is analyzed using all 100.000 data points per shot and by downsampling to 50.000, 20.000 and 10.000 yielding a ToF resolution of 2, 4, 10 and 20 ns respectively. Firstly, charge-state-resolved and total recovered energy are compared for the original and alternative binning methods discussed in Section 6.1.1 for a time resolution of 20 and 2 ns.

Figure 6.4 shows four comparisons of the different binning methods. For all methods, including the original binning method, a decrease in charge-state-resolved energies is observed. This decrease is mainly observed at the higher charge states, which is explained by the fact that higher charge states have larger kinetic energies on average. High energy ions are measured in energy bins containing fewer ToF points. The sub-binning methods show a larger deviation between the two ToF resolutions due to numerical

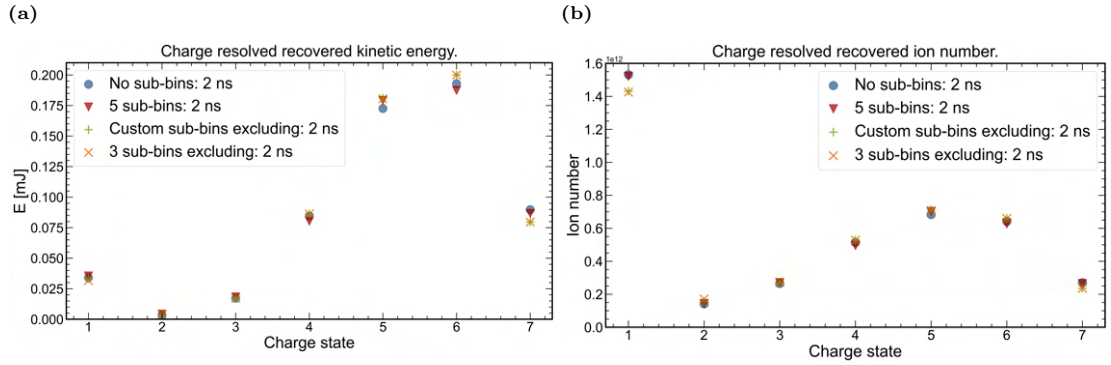

Figure 6.3.: Recovered charge-state-resolved energy (a) and ion number (b) for three alternatives to conventional binning using a ToF resolution of 2 ns. The alternative binning methods are: the use of 5 sub-bins, a custom number of sub-bins and 3 sub-bins. For the last two binning methods the extrema sub-bins are excluded from analysis.

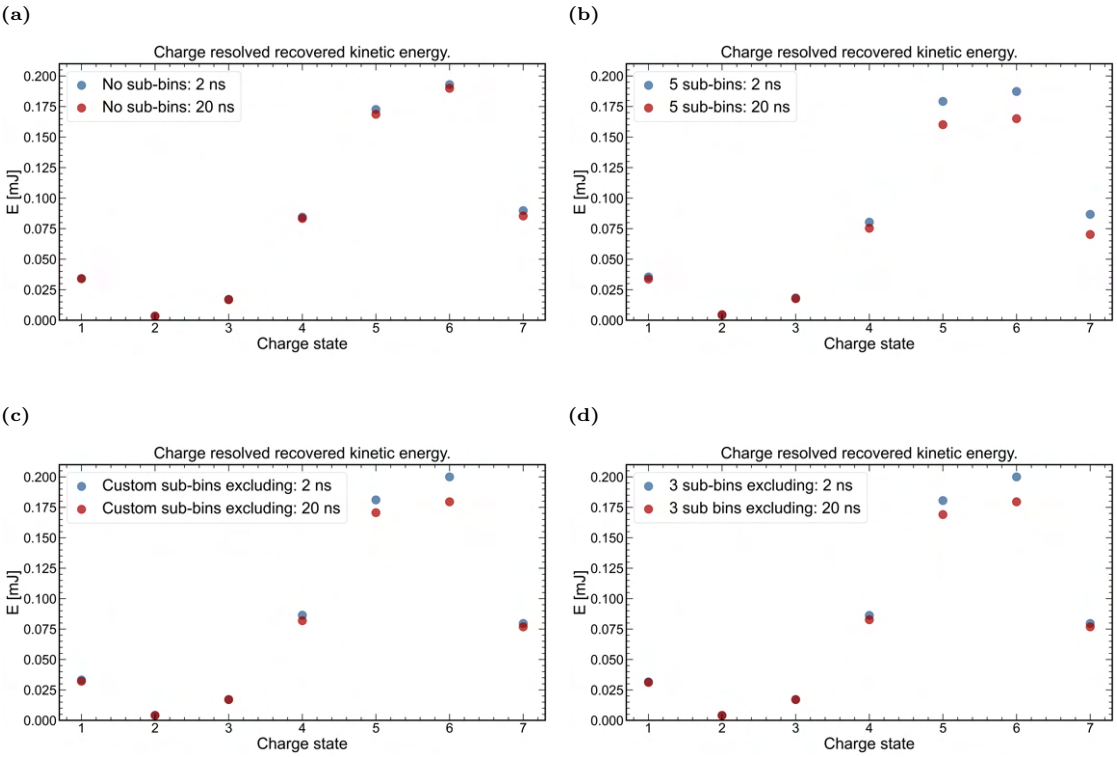

Figure 6.4.: Comparison of charge-state-resolved recovered energy using four binning methods. For each method the use of a time-of-flight resolution of 2 ns is compared to a resolution of 20 ns. (a) shows the original binning method. (b) shows the use of 5 sub-bins. (c) shows the use of a custom number of sub-bins and (d) shows the use of 3 sub-bins. For the last two methods the exclusion of extrema sub-bins has been implemented.

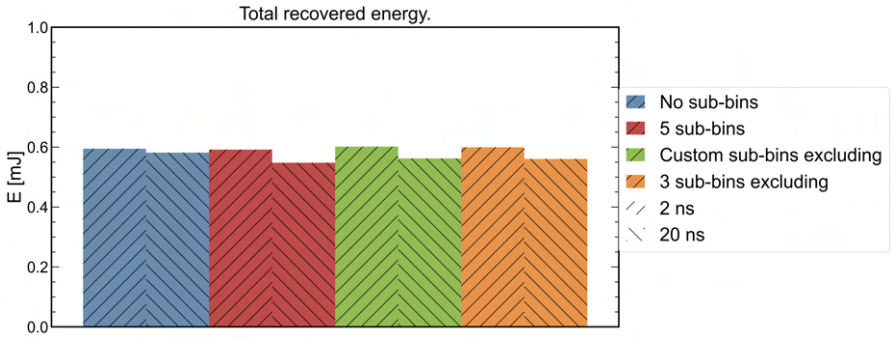

Figure 6.5.: Total recovered energy for four different binning methods, using a time-of-flight resolution of 2 ns (slanted up) and 20 ns (slanted down). A decrease in recovered total energy is observed for all binning methods when a resolution of 20 ns is used.

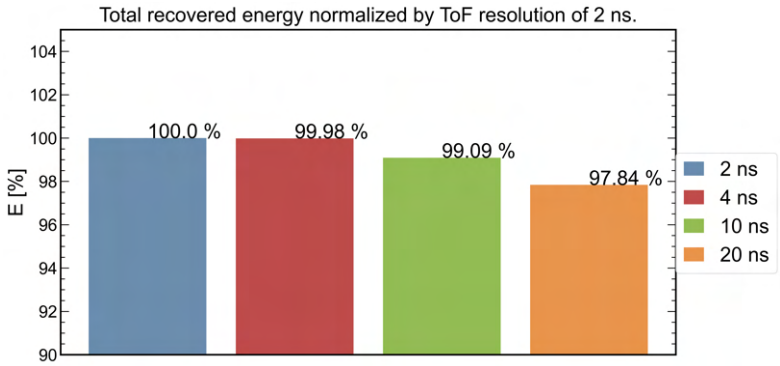

Figure 6.6.: Total energy for four time-of-flight resolutions, normalized by the energy calculated with a resolution of 2 ns.

instability, in line with the simulation results. More and thus smaller sub-bins show a larger deviation, again in agreement with numerical instability due to a ToF resolution that is too coarse.

Figure 6.5 shows a comparison of the total recovered energies using the a ToF sampling rate of 2 and 20 ns. For all binning methods a decrease in recovered total energy can be observed with the coarser resolution. For the original binning method the total ion number, energy, and momentum are all roughly 2 % less when a ToF sampling rate of 20 ns is used compared to 2 ns.

The largest deviation in ion energy is observed between the custom binning method using a ToF resolution of 2 ns and the use of 5 sub-bins with a resolution of 20 ns. The total recovered energy is 9 % lower, when using the latter compared to the former.

The ToF resolution influencing the spectra and calculated ion figures is undesirable. Increasing the resolution seems preferable based on simulations. In simulations the spectra and calculated energies converge to the input value as the ToF resolution is increased from 20 to 2 ns. Four ToF resolutions are compared to investigate the experimental sensitivity to ToF resolution. The resolutions 2, 4, 10 and 20 ns are studied, using the conventional binning method. Figure 6.6 shows the comparison, a ToF resolution of 4 ns gives a total energy that is very similar to the use of 2 ns, only differing by 0.02 %. The 10 and 20 ns resolutions recover 0.91 % and 2.16 % less total energy respectively. Note that this reduction in total energy is observed without the use of sub-bins. Doubling the time resolution from 20 to 10 ns influences the recovered energy more than doubling from 4 to 2 ns, which could indicate that using a resolution of 2 ns has diminishing returns when compared to 4 ns.

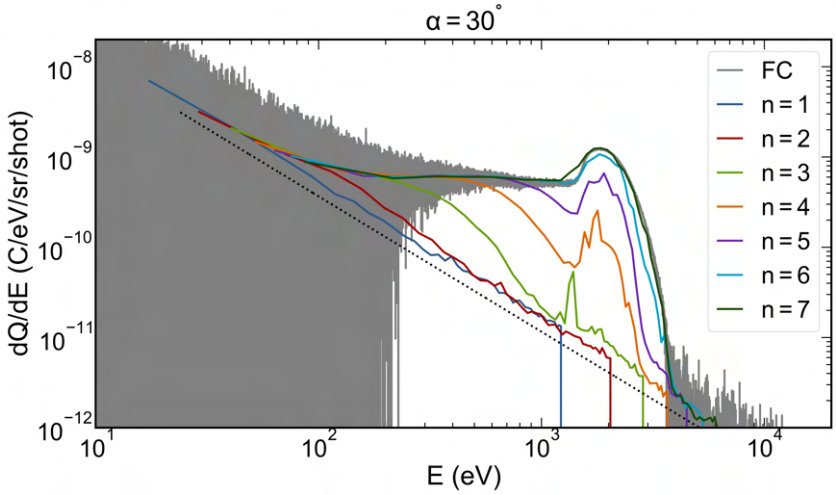

Figure 6.7.: Cumulative spectra obtained in the experimental test, employing conventional binning with a ToF resolution of 2 ns. Black dotted line is proportional to $E^{-\frac{3}{2}}$.

6.2. Cumulative spectra

The Sn^{1+} ion number shown in Figure 6.3b seems to be an outlier, when compared to the remaining charge states. The ion number seems to resemble a (left skewed) probability distribution with Sn^{5+} as the most likely charge state. To investigate what causes this potential outlier the cumulative spectra are investigated. In Figure 6.7 the cumulative spectra obtained in the experimental test is shown. The spectra are obtained using conventional binning, using the time resolution of 2 ns. The black dotted line is proportional to $E^{-\frac{3}{2}}$. As observed in the forward simulations, a noise floor of this shape appears when white noise is applied. The first cumulative spectrum is almost perfectly parallel to this power law. This could mean that in the analysis of the current experimental test much of the assigned current of Sn^{1+} is due to noise and not recorded ionic emission. The second cumulative spectrum shows a similar shape, with a small hump which could correspond to recorded Sn^{2+} emission on top of the same noise floor as the first cumulative spectrum. To obtain the second charge resolved spectrum the noise floor is subtracted, thus the second charge state is likely less affected by the artificial increase.

6.3. Discussion of experimental results

Experimental measurements were taken to investigate the effect of sub-binning on experimental data. With the knowledge obtained from earlier work and analysis (Chapter 2 and 3) and forward simulations (Chapter 4 and 5), alternatives to conventional binning were studied.

Three alternatives are investigated, one employing all sub-bins and two where the two extrema sub-bins are excluded from analysis. For the first, 5 sub-bins were used leading to a sawtooth pattern on the charge-resolved spectra in agreement with simulations. For the second analysis, based on the simulations, a custom number of sub-bins was used per bin. The exclusion of the extrema sub-bins leads to a reduction in the sawtooth pattern. For the final analysis, 3 sub-bins were used with the two extrema sub-bins excluded. Unsurprisingly this completely remedies the sawtooth pattern, as the number of assigned points in this method is the same as the original method.

For all alternative binning methods, the charge resolved and total ion number, energy and momentum were calculated. For all considered alternatives the change in charge-state-resolved energy is of order of 0.01 mJ ($\approx 1.7\,\%$ of E_{tot}), when compared to the original binning method. The total recovered energy and momentum increase slightly by roughly 1 % and 0.5 % respectively, while the ion number is reduced by roughly 1 % with the binning + exclusion methods, when compared to conventional binning. The use of all 5 sub-bins has an even smaller effect on the total numbers.

In the experimental data considered, the Bottom-Up method is surprisingly robust to binning method with a ToF resolution of 2 ns. The recovered ion figures are nearly unchanged even with exclusion of $\frac{2}{3}$ of the data at the extrema of the energy bins.

A comparison of the use of a ToF resolution of 20 and 2 ns has been performed additionally. For this comparison the same data has been used, downsampling to obtain the former resolution. The use of the 20 ns resolution leads to a decrease in recovered energy, in agreement with the forward simulations. In the forward simulations this decrease is caused by numerical instability and represents a worse reconstruction. When comparing the time resolutions for the original binning method, the 20 ns resolution leads to a decrease in total energy of roughly 2 %.

Remarkably, in the experimental test the use of sub-bins (and excluding extrema sub-bins) has a smaller effect on total recovered energy than the ToF resolution using conventional binning. In experiments the actual total kinetic energy is not known, therefore is not possible to definitively say that one ToF resolution is better based on experimental analysis alone. In forward simulations recovered energy improves with a 2 ns ToF resolution. It is plausible that total ion number, kinetic energy, and momentum are underestimated by roughly 1 to 2 % percentage points with a 20 ns resolution. The underestimation would be mainly due to underestimation of higher charge states, as these distributions are located at a higher kinetic energy. Higher energies are most affected by numerical instability in the Bottom-Up method.

For the sake of completeness: in this work only the 30° angle was analysed to reduce computational time. The use of only this angle might have introduced a bias in the results presented. While the author sees no reason that the other larger measurement angles would show a higher sensitivity, this intuition might prove false. Larger angles lack or have a smaller high-energy peak, which likely would lead to smaller deviations in total recovered energy as less highly energetic ions are measured at these angles.

7. Conclusions

The Bottom-Up method is an analysis method that is used to obtain charge-state-resolved energy spectra of ion emission from (tin) laser produced plasmas. Ionic emission is recorded using retarding field analyzers. The measurement procedure and analysis could introduce systematic effects/errors that might influence the recovered spectra, reducing their fidelity. In this work, a combination of simulations and experimental data was employed to investigate these effects.

Chapter 2 gives an explanation of the measurement of ionic emission using retarding field analyzers (RFAs). Potential errors and uncertainties that might arise using this measurement method are discussed. Five experimental systematic effects are identified that might introduce uncertainty about charge state, energy and/or ion current. These are the spread in isotope mass, the energy resolution of an RFA, the transmission function of an RFA, experimental noise, and drift and acceleration due to the RFA potentials.

Chapter 3 explains the Bottom-Up analysis method that is used to analyzed RFA time-of-flight data. Systematic errors introduces by the Bottom-Up method are presented. The method can lead to a broadening of peaks and a reduction of peak height due to binning of current. Subdividing the energy bins, known as sub-binning, can mitigate these effects.

Motivated by identified systematic effects, so-called 'forward simulations' were performed with predetermined energy spectra. The forward simulations are explained in **Chapter 4** and the results presented and discussed in **Chapter 5**. The forward simulations allow the performance of an in-depth study of the magnitude of systematic effects relevant to the Bottom-Up method. The use of a retarding field analyzer in time-of-flight mode to obtain charge-state-resolved spectra of ions emitted from (tin) laser produced plasmas, has been investigated. The forward simulations are performed by simulating RFA measurements on predetermined energy spectra. The simulated time-of-flight data is used as an input for the Bottom-Up method.

The effects included in simulations are: spread in tin isotope mass, experimental noise, energy resolution and transmission function of an RFA. These effect have been studied individually, benchmarked against an idealized simulation, where none of the effects have been included. In these simulations the Bottom-Up method is robust under the effects studied on the whole, being able to output a charge state sum and charge-state-resolved spectra that resemble the input data with high fidelity. Different charge states and energy ranges are affected more strongly by certain systematic effects than others however. The effects lead in some cases to an over- or underestimation of assigned ion current and thereby recovered energy. For all studied individual effects the difference in the recovered energy is in the single digit percentage points, compared to the ideal simulation. The transmission function has the largest effect on recovered energy. Simulating a transmission similar to an experimentally measured transmission function leads to an increase in total recovered energy of 5 %pt when compared to an ideal simulation without experimental systematic effects.

Additionally, three potential improvements to the measurement procedure have been investigated using forward simulations. The potential improvements are an increased number of retarding voltages, alternative spacing between retarding voltages and the use of sub-binning. The first two have negligible effect on charge-state-resolved and total energy. Simulations without experimental systematic effects show that sub-binning can lead to an improved reconstruction of spectra when a sufficiently fine time-of-flight resolution is employed. A time resolution that is too coarse can lead to numerical instability, underestimating ion current and subsequently ion number, energy and momentum. The numerical instability is most pronounced at high energy, as higher charge states have distributions that peak at higher energies, this leads to the underestimation mainly of the higher charge states. In the simulations the experimental resolution limit of 2 ns is sufficiently fine. Using this resolution of 2 ns the deviation between input and recovered energy reduces from 2 to 0.5 % when sub-binning is employed compared to conventional binning.

Including all studied systematic experimental effects leads to a "realistic simulation". To prevent numerical instability influencing the results the ToF resolution of 2 ns has been used for these realistic simulations. When sub-binning is applied on realistic simulations, a sawtooth pattern appears over the

charge-state-resolved spectra. The sawtooth pattern is caused by the fact that most of the systematic effects affect the sub-bins at the extrema of an energy bin more than the central sub-bins. In particular, the spread in isotope mass, energy resolution and transmission of the RFA cause the pattern in the simulations. To mitigate this effect, excluding the extrema sub-bins has been investigated. This leads to a reduction in the sawtooth pattern and an improved reconstruction of input charge-state-resolved spectra. This improved reconstruction indicates that the recovery of charge-state-resolved spectra in experimental data might be improved by sub-binning and excluding the extrema to avoid contamination of charge states. Using a custom number of sub-bins based on bin number and excluding extrema gives an improved reconstruction. The deviation in total recovered energy reduces from 2.5 to 1.5 % when this custom-binning method is used, when compared to the conventional binning method.

Subsequently, experimental data has been investigated to validate the simulations (**Chapter 6**). Applying sub-binning on experimental data shows a sawtooth pattern similar to the realistic simulations. This indicates a match between the forward simulation model and reality. Furthermore, excluding the extrema sub-bins reduces/removes the sawtooth, in agreement with simulations. Three alternative binning methods are investigated, in all cases the recovered total energy changes by roughly 1 % compared to conventional binning. This fact holds true even when the first and last $\frac{1}{3}$ of the energy bins are excluded, where assigned charge state is most uncertain.

From the experimental tests, the viability of sub-binning has been shown; however, the effect of sub-binning on total recovered energy was found to be negligible. Sub-binning is more computationally expensive and requires a higher sampling rate than conventional binning. The increased sampling means that more data needs to recorded and stored, while the result does not deviate significantly.

Based on both simulations and experimental work performed the effect of the (uncertain) bin extrema regions on recovered total energy is minute. Ion current might be incorrectly assigned but on the whole the spectra are only marginally influenced. Noise can increase the ion energy and number of Sn^{1+} significantly. The current work has shown that the use of the middle of 3 sub-bins yield spectra very similar to using the entire bin. The use of alternative binning methods might lead to a more significant change in recovered energy for plasmas emitting higher charge states. As energy resolution, isotope mass spread and transmission affect an increasing fraction of the bin with increased charge state. Excluding the extrema sub-bins might then prove more important to accurately distinguish charge states.

Downsampling ToF resolution was implemented on experimental data based on observations from the forward simulations. This downsampling is motivated by the observation that the ToF resolution of 20 ns leads to numerical instability. Numerical instability influences spectra and recovered energy even without the use of sub-bins in simulations. Downsampling allows the comparison of a single data set with the use of different ToF resolutions. A comparison of ToF resolutions between 2 to 20 ns shows a significant effect on charge-state-resolved and total recovered energy in line with simulations. A decrease in recovered energy is observed using the most coarse ToF resolution. The highest charge states are most affected by ToF resolution. High energy current is most affected by numerical instability and higher charge states have higher energy on average. Total recovered energy is roughly 2.2 % lower using the 20 ns resolution compared to the 2 ns resolution.

7.1. Outlook and future research

The geometric transmission of the RFA could introduce uncertainty in recorded current, as it has been found that the grids are randomly placed in some RFAs and perfectly aligned in other RFAs. This alignment leads to a geometric transmission that can range between roughly 40 to 80 %. As the method makes use of a correction factor for transmission of randomly placed grids, this could lead to a overestimation in current of roughly 100 % in for a geometric tranmission of 80 %. A study of individual RFAs might lead to an improved transmission correction factor for each individual RFA. This might be done with the use of photography to record relative alignment or with the use of a ion source with a known ion flux.

In the simulations where noise has been included, a noise floor ($\propto E^{-\frac{3}{2}}$) appears on the spectrum of Sn^{1+}. Noise leads to a large increase in ion number and energy for Sn^{1+}. This increase is due to the fact that for the first charge state, there is no earlier cumulative spectrum which is subtracted. The method treats all negative current as non-physical, this has the effect that only positive values of noise contribute. All charge-state-resolved spectra except the first are obtained by the subtraction of a cumulative spectrum

including the noise floor. In the experimental data used in this work, the Sn^{1+} spectrum seems featureless, seeming to follow a power law reminiscent of the noise floor. It is plausible that hardly any Sn^{1+} ions are emitted and that a significant fraction of assigned Sn^{1+} ion number, kinetic energy and momentum is due to noise. The minute number of recovered Sn^{2+} ions with respect to all other charge states and in particular Sn^{1+} also points to this possibility. Looking at the ion numbers as (proportional to) a probability distribution, Sn^{5+} seems the most likely charge state, with the probability falling off in both directions. The Sn^{1+} is an outlier if looked at in this way. Future work could focus on the subtraction of the noise level. This might be done by utilizing the data in the 'zeroth bin', which is energy bin where no ions should be able to be measured. By subtracting the 'cumulative zeroth spectrum' from the the $\frac{\mathrm{d}Q_{n=1}}{\mathrm{d}E}$ spectrum an improved reconstruction might be possible. Another possibility is an alternative calculation of mean current which includes negative values due to noise. In this alternative approach negative mean current could be treated as non-physical, rather than all negative current.

Future experimental research can employ the Bottom-Up method with the knowledge that the systematic effect at the bin edges lead to a marginal change of roughly 1 to 2 % in the charge resolved and total ion number, energy or momentum for LPPs with charge states until 7 measured at 30°. Spectra obtained from LPPs with higher charge states and other angles with respect to the laser might have a different dependence and could merit further investigation. A time resolution of 20 ns has been shown to be insufficient in simulations and to lead to deviations in experimentally obtained spectra and energies when compared to a resolution of 2 ns.

Future work could benefit from an increased ToF resolution, keeping in mind that additional computational time and storage are required due to the larger data sets. A resolution of 4 ns yielded a very similar experimental result in the current work. Using a resolution of 4 ns corresponds to half the storage of a 2 ns resolution. Further research could investigate the sensitivity of spectra and charge-state-resolved and total energy on ToF resolution in more detail to balance the effect of numerical instability against storage and computational time.

Bibliography

[1] J. W. Lathrop, "The diamond ordnance fuze laboratory's photolithographic approach to microcircuits", IEEE annals of the history of computing **35**, 48–55 (2013) (cited on page 1).

[2] S. Rai, "Ionic interactions around euv generating tin plasma", PhD thesis (University of Groningen, 2023) (cited on pages 1–2).

[3] D. J. Hemminga, O. Versolato, and J. Sheil, "Simulations of plasmas driven by laser wavelengths in the 1.064—10.6 μm range for their characterization as future extreme ultraviolet light sources", Physics of Plasmas **30**, 10.1063/5.0125936 (2023) (cited on page 1).

[4] R. Schupp, F. Torretti, R. Meijer, M. Bayraktar, J. Sheil, J. Scheers, D. Kurilovich, A. Bayerle, A. A. Schafgans, M. Purvis, K. Eikema, S. Witte, W. Ubachs, R. Hoekstra, and O. Versolato, "Radiation transport and scaling of optical depth in nd:yag laser-produced microdroplet-tin plasma", Applied Physics Letters **115**, 124101 (2019) (cited on page 1).

[5] O. Versolato, "Physics of laser-driven tin plasma sources of euv radiation for nanolithography", Plasma Sources Science and Technology **28**, 083001 (2019) (cited on pages 1–2).

[6] L. Poirier, "Ion diagnostics for extreme ultraviolet nanolithography", PhD thesis (Vrije Universiteit Amsterdam, 2023) (cited on pages 1, 5).

[7] D. B. Abramenko, M. Spiridonov, P. V. Krainov, V. M. Krivtsun, D. Astakhov, M. Van Kampen, D. Smeets, and K. N. Koshelev, "Measurements of hydrogen gas stopping efficiency for tin ions from laser-produced plasma", Applied Physics Letters **112**, 10.1063/1.5025914 (2018) (cited on pages 1–2).

[8] J. R. Freeman, S. S. Harilal, B. Verhoff, A. Hassanein, and B. Rice, "Laser wavelength dependence on angular emission dynamics of nd : yag laser-produced sn plasmas", Plasma Sources Science and Technology **21**, 055003 (2012) (cited on page 1).

[9] G. J. Tallents, "On the fitting of displaced maxwellians to laser-produced plasma ion velocity distributions", Optics Communications **37**, 108–112 (1981) (cited on pages 1, 17).

[10] S. Fujioka, M. Shimomura, Y. Shimada, S. Maeda, H. Sakaguchi, Y. Nakai, T. Aota, H. Nishimura, N. Ozaki, A. Sunahara, K. Nishihara, N. Miyanaga, Y. Izawa, and K. Mima, "Pure-tin microdroplets irradiated with double laser pulses for efficient and minimum-mass extreme-ultraviolet light source production", Applied Physics Letters **92**, 10.1063/1.2948874 (2008) (cited on page 1).

[11] D. J. Hemminga, L. Poirier, M. M. Basko, R. Hoekstra, W. Ubachs, O. Versolato, and J. Sheil, "High-energy ions from nd:yag laser ablation of tin microdroplets: comparison between experiment and a single-fluid hydrodynamic model", Plasma Sources Science and Technology **30**, 105006 (2021) (cited on pages 1–2, 17).

[12] . Borisov, A. Eltzov, A. S. Ivanov, O. B. Khristoforov, Y. Kirykhin, A. Y. Vinokhodov, V. A. Vodchits, V. Mishhenko, and A. V. Prokofiev, "Discharge produced plasma source for euv lithography", Proceedings of SPIE, 10.1117/12.740590 (2007) (cited on page 1).

[13] Y. Tao and M. S. Tillack, "Mitigation of fast ions from laser-produced sn plasma for an extreme ultraviolet lithography source", Applied Physics Letters **89**, 10.1063/1.2349831 (2006) (cited on pages 1–2).

[14] D. Kurilovich, A. L. Klein, F. Torretti, A. Lassise, R. Hoekstra, W. Ubachs, H. Gelderblom, and O. Versolato, "Plasma propulsion of a metallic microdroplet and its deformation upon laser impact", Physical review applied **6**, 10.1103/physrevapplied.6.014018 (2016) (cited on page 1).

[15] L. Poirier, A. Bayerle, A. Lassise, F. Torretti, R. Schupp, L. Behnke, Y. Mostafa, W. Ubachs, O. Versolato, and R. Hoekstra, "Cross-calibration of a combined electrostatic and time-of-flight analyzer for energy- and charge-state-resolved spectrometry of tin laser-produced plasma", Applied Physics B **128**, 10.1007/s00340-022-07767-1 (2022) (cited on pages 2, 5, 8, 11, 17).

[16] S. Rai, K. Bijlsma, L. Poirier, E. De Wit, L. Assink, A. Lassise, I. Rabadán, L. Méndez, J. Sheil, O. Versolato, and R. Hoekstra, "Evidence of production of kev sn+ ions in the h2 buffer gas surrounding an sn-plasma euv source", Plasma sources science technology **32**, 035006 (2023) (cited on page 2).

[17] Burdt, "Ion emission and expansion in laser-produced tin plasma", PhD thesis (UC San Diego, 2011) (cited on page 2).

[18] L. Poirier, D. J. Hemminga, A. Lassise, L. Assink, R. Hoekstra, J. Sheil, and O. Versolato, "Strongly anisotropic ion emission in the expansion of nd:yag-laser-produced plasma", Physics of Plasmas **29**, 10.1063/5.0129112 (2022) (cited on pages 2, 11, 14, 17).

[19] *Detector faraday cup fc73*, 2023 (cited on page 5).

[20] L. Assink, "Design analyses for a new experimental rig to study the energy loss of sn ions in h2 gas", MSc thesis (University of Groningen, 2022) (cited on pages 6, 8–9, 11, 19, iii).

[21] L. Poirier, A. Lassise, Y. Mostafa, L. Behnke, N. Braaksma, L. Assink, R. Hoekstra, and O. Versolato, "Energy- and charge-state-resolved spectrometry of tin laser-produced plasma using a retarding field energy analyzer", Applied Physics B **128**, 10.1007/s00340-022-07844-5 (2022) (cited on pages 11, 17, 27).

[22] R. Burdt, Y. Ueno, Y. Tao, S. Yuspeh, M. S. Tillack, and F. Najmabadi, "Recombination effects during expansion into vacuum in laser produced sn plasma", Applied Physics Letters **97**, 10.1063/1.3473817 (2010) (cited on page 17).

[23] J. Sheil, L. Poirier, A. Lassise, D. Hemminga, S. Schouwenaars, N. Braaksma, A. Frenzel, R. Hoekstra, and O. Versolato, "Invariance of the charge state dependence on kinetic energy in expanding laser-produced plasmas", 2024, in preparation (cited on page 27).

A. Appendices

A.1. Maximal distinguishable charge-state

The Bottom-Up method makes use of RFA data, using this we are able to distinguish charge states. To do so we make some assumptions, one of these assumptions is that the mass of each tin ion is the same, namely the abundance weighted average mass: 118.71 u. However in reality, tin has a 10 stable isotopes masses. This fact introduces a spread in times-of-flight that correspond to the same kinetic energy. Put differently a heavier isotope will have a higher kinetic energy than a lighter isotope for the same ToF.

The criterion for passing the retarding voltage is

$$E > zeU_{\mathrm{ret}}, \tag{A.1}$$

where E is the kinetic energy

$$E = \frac{1}{2}mv^2 = \frac{1}{2}m\frac{L^2}{t^2}. \tag{A.2}$$

Given a certain kinetic energy the time-of-flight is given by

$$t = L\sqrt{\frac{m}{2E}}. \tag{A.3}$$

Only ions with sufficient kinetic energy to pass the retarding potential are measured. The cutoff in potential ToF for a certain charge state with a given mass to be measured is

$$t^z_{\mathrm{max}}(m) = L\sqrt{\frac{m}{2zeU_{\mathrm{ret}}}}, \tag{A.4}$$

$$t^z_{\mathrm{max}}(m) \propto \sqrt{\frac{m}{z}}. \tag{A.5}$$

However the cutoff time will have a spread, with the actual value depending on the spread in mass of different isotopes. As every term for a given measurement is proportional to L and inversely proportional to $\sqrt{2eU_{\mathrm{ret}}}$ these terms will cancel out. Without loss of generality then, we can simplify the expression by defining $L = 1$, $\frac{1}{\sqrt{2eU_{\mathrm{ret}}}} = 1$, as these are the same for each isotope in a single shot. We obtain:

$$t^z_{\mathrm{max}}(m) = \sqrt{\frac{m}{z}}. \tag{A.6}$$

The spread in t_{max} is given by

$$\Delta t^z_{\mathrm{max}} = \sqrt{\frac{\Delta m}{z}}. \tag{A.7}$$

Overlap occurs when the heaviest ions of charge state z+1 have the same t_{max} as the lightest of charge state z, thus

$$t^z_{\mathrm{max}}(m^-) = t^{z+1}_{\mathrm{max}}(m^+), \tag{A.8}$$

$$\sqrt{\frac{m^-}{z}} = \sqrt{\frac{m^+}{z+1}}, \tag{A.9}$$

$$\frac{m^-}{z} = \frac{m^+}{z+1}, \tag{A.10}$$

$$\frac{m^+}{m^-} = \frac{z+1}{z}. \tag{A.11}$$

Filling in the value of the lightest and isotope of tin, 111.9 and 123.9 u respectively

$$\frac{123.9}{111.9} = \frac{z+1}{z} = 1.107, \tag{A.12}$$

$$z + 1 = 1.107z, \tag{A.13}$$

$$1 = 0.107z, \tag{A.14}$$

$$z = \frac{1}{0.107} = 9.325. \tag{A.15}$$

The above means that the least massive charge state 9.325 and most massive charge state 10.325 would become indistinguishable. However as charge states only take on integer values, experimentally charge states 10 and 11 will become indistinguishable. As a light Sn^{11+} can arrive before a heavy Sn^{10+}. In general charge states will become indistinguishable when

$$z = \frac{1}{\frac{m^+ - m^-}{m^-}} = \frac{1}{\frac{\Delta m}{m^-}} = \frac{m^-}{\Delta m}. \tag{A.16}$$

Given a single isotope, $\Delta m = 0$. Taking the limit of Δm to 0, the maximal charge state that we can distinguish diverges to infinity

$$\lim_{\Delta m \to 0^+} z = \lim_{\Delta m \to 0} \frac{m^-}{\Delta m} = \infty. \tag{A.17}$$

In theory for a single isotope all charge states are distinguishable based on the cutoff time. Experimentally however, for very high charge states the difference in cutoff time of subsequent charge states will become very small, in which case the destructibility will be limited by the time resolution of the measurement device.

A.2. Drift and acceleration

When measuring with a Faraday cup without (retarding) potentials the transformation from time-of-flight to kinetic energy is straightforward if mass and distance are known. As the velocity is constant over the whole flight and we simply have

$$t = \frac{l_0}{v_0} = l_0\sqrt{\frac{m}{2E_0}} \tag{A.18}$$

where l_0 is the distance from the LPP to the FC and v_0 is the initial (and constant) velocity of the particle.

As the retarding field analyzers contains biased grids, the potential is not isotropic. Electric fields exist in the RFA between the grids, which can accelerate or decelerate charged particles. The expression for time-of-flight becomes [20]

$$\tau = (\frac{l_1}{l_0} + \frac{2}{1+\sqrt{1-\frac{qU_{\text{ret}}}{E_0}}}\frac{l_2}{l_0} + \frac{1}{\sqrt{1-\frac{qU_{\text{ret}}}{E_0}}}\frac{l_3}{l_0} + \frac{2}{\sqrt{1-\frac{qU_{\text{ret}}}{E_0}}+\sqrt{1-\frac{qU_S}{E_0}}}\frac{l_4}{l_0} + \frac{2}{\sqrt{1-\frac{qU_S}{E_0}}+\sqrt{1-\frac{qU_C}{E_0}}}\frac{l_5}{l_0} + \frac{1}{\sqrt{1-\frac{qU_c}{E_0}}}\frac{l_6}{l_0})\frac{l_0}{v_0}. \tag{A.19}$$

Where the different values of l_i correspond to the distance from LPP to the first grid (ground) and distance traveled between grids and to the FC. For experimentally used values of retarding, suppressor and cup voltage this may introduce additional time-of-flight for ions know as drift. This drift effect is most pronounced for ions that just barely have enough kinetic energy to pass the potential barrier. We can see this from the second and third term, if the pass energy E_0 is just larger than qU_{ret} then the fraction $\frac{qU_{\text{ret}}}{E_0}$ becomes very nearly 1, in turn the whole argument of the square root becomes very nearly 0. The fraction diverges and the time-of-flight is increased signifiantly, which is known as drift.

Time-of-flight can also be decreased due to the potentials for particles that more easily pass the potential barrier. These particles can get accelerated by the suppressor and biased cup leading to a reduced flight time. The effect is most pronounced when the absolute value of the retarding voltage is small compared to the absolute value of the suppressor (and cup voltage) as they are of the opposite polarity. This is show in Figure A.1a, where $\frac{\tau}{t}$ is shown for different initial energies for a retarding potential of 50 V. The analytical flight time, τ is divided by the potential free flight time, t. Drift occurs if $\frac{\tau}{t}$ is greater than 1, acceleration means that $\frac{\tau}{t}$ is less than 1.

Two examples are shown in Figure A.1, experimental potential values have been used and the distances between the grids also correspond to the Kimball FC73-A. Note that for lower values of retarding voltage that only ions with initial kinetic energies slightly above the effective potential, drift occurs. At higher energies acceleration due to the suppressor and FC, becomes dominant. At higher retarding voltages the effect of drift becomes dominant as the retarding voltage is (much) larger than the suppressor and FC potentials. For all retarding voltages, as the initial energy becomes higher, the effect of the RFA on ToF decreases.

(a)

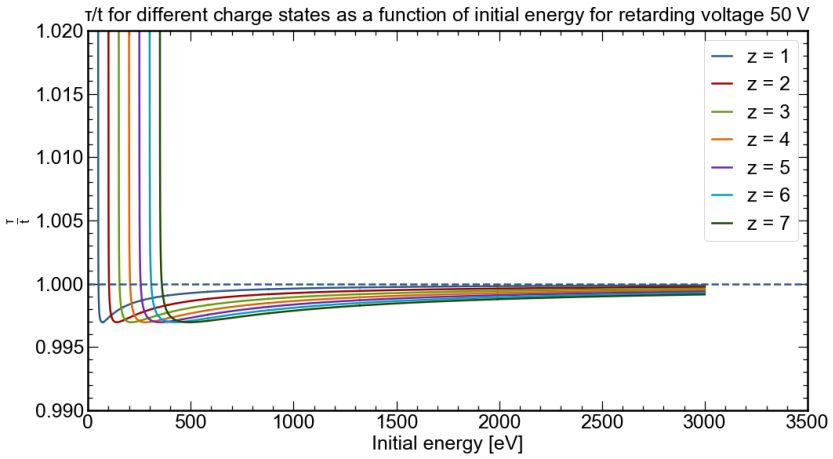

(b)

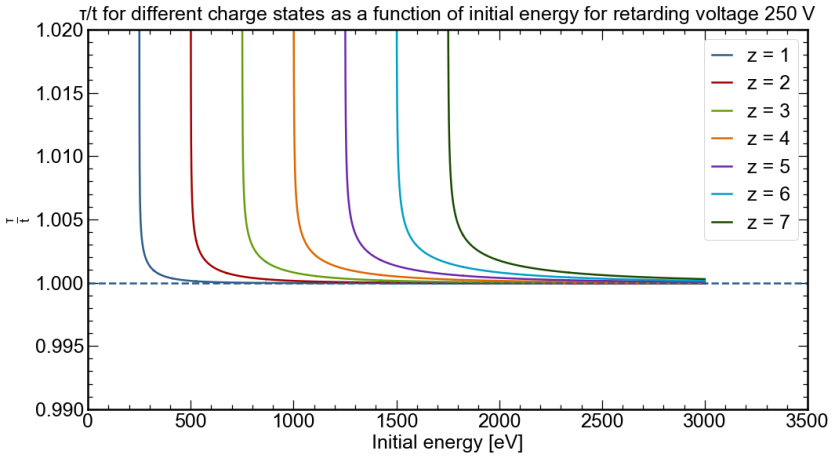

Figure A.1.: Two examples of analytical time-of-flight (ToF) normalized by the potential free time-of-flight. A ToF above corresponds to an increased ToF due to the potential, known as drift. A ToF below 1 corresponds to a decreased ToF, known as acceleration. In (a) a retarding voltage of 50 V has been used, in (b) a retarding voltage of 250 V has been used. The remaining potentials correspond to those used experimentally, a suppressor potential of −100 V and a cup bias of −30 V.